

# A locally stabilized immersed boundary method for the compressible Navier–Stokes equations



C. Brehm <sup>a,\*</sup>, C. Hader <sup>b</sup>, H.F. Fasel <sup>b</sup>

<sup>a</sup> Science and Technology Corporation, NASA Ames, Moffett Field, CA 94035, USA

<sup>b</sup> University of Arizona, Tucson, AZ, USA

## ARTICLE INFO

### Article history:

Received 28 July 2014

Received in revised form 23 January 2015

Accepted 18 April 2015

Available online 23 April 2015

### Keywords:

Immersed boundary

Higher-order finite-difference

Numerical stability analysis

Compressible flows

## ABSTRACT

A higher-order immersed boundary method for solving the compressible Navier–Stokes equations is presented. The distinguishing feature of this new immersed boundary method is that the coefficients of the irregular finite-difference stencils in the vicinity of the immersed boundary are optimized to obtain improved numerical stability. This basic idea was introduced in a previous publication by the authors for the advection step in the projection method used to solve the incompressible Navier–Stokes equations. This paper extends the original approach to the compressible Navier–Stokes equations considering flux vector splitting schemes and viscous wall boundary conditions at the immersed geometry. In addition to the stencil optimization procedure for the convective terms, this paper discusses other key aspects of the method, such as imposing flux boundary conditions at the immersed boundary and the discretization of the viscous flux in the vicinity of the boundary. Extensive linear stability investigations of the immersed scheme confirm that a linearly stable method is obtained. The method of manufactured solutions is used to validate the expected higher-order accuracy and to study the error convergence properties of this new method. Steady and unsteady, 2D and 3D canonical test cases are used for validation of the immersed boundary approach. Finally, the method is employed to simulate the laminar to turbulent transition process of a hypersonic Mach 6 boundary layer flow over a porous wall and subsonic boundary layer flow over a three-dimensional spherical roughness element.

© 2015 Elsevier Inc. All rights reserved.

## 1. Introduction and motivation of the research

Immersed Boundary Techniques (IBTs) have been developed for many years and have appeared in various forms since they were first introduced by Peskin [1,2] (see for example Goldstein et al. [3], LeVeque and Li [4], Wiegmann and Bube [5], Linnick and Fasel [6], Johansen and Collela [7], Mittal and Iaccarino [8], Zhong [9], Duan et al. [10] and many others). These methods were first introduced as a nontraditional approach for numerically solving initial/boundary-value problems for complex geometries and have matured to become increasingly important for a wide range of applications [11–13]. Fig. 1 shows a 2D example of an arbitrary immersed boundary cutting through a Cartesian grid. A major advantage of these methods is their simplicity in generating grids independent of the complexity of the geometry. The grid-generation process for body-fitted structured or unstructured grids for complex geometries is generally very laborious because the process aims

\* Corresponding author.

E-mail addresses: christoph.brehm@nasa.gov, cbrehm@email.arizona.edu (C. Brehm).

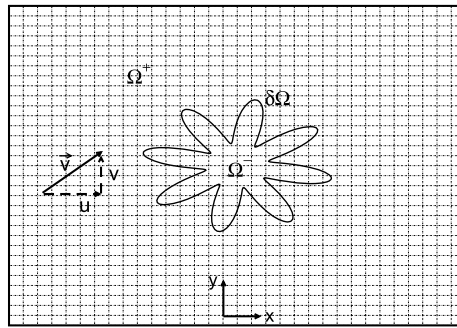


Fig. 1. Arbitrary geometry immersed into a Cartesian grid.

at generating well behaved grids that have sufficient local resolution while minimizing the total number of required grid points. Except for the simplest geometries, these conflicting requirements can lead to deterioration in grid quality, thereby negatively impacting the accuracy and convergence properties of the flow solver (see Ferziger and Peric [14]). For highly complex geometries, which are relevant for many fields of science and engineering, the process of generating a high-quality grid is extremely time consuming. For flows involving moving and deforming boundaries, IBTs also provide clear advantages over classical body fitted grid approaches. Simulating such flows on body-fitted grids requires generating a new grid at each time step, in addition to requiring a procedure to project the solution onto this new grid (Tezduyar [15]). These two characteristics of body-fitted grids associated with simulating flows with moving and deforming boundaries may negatively impact the accuracy, robustness, and computational cost of the numerical solution method. Particularly, in cases where the boundary exhibits large motions, body-conformal grid strategies cause immense difficulties in the solution procedure. This is where an immersed boundary approach with its fully Eulerian approach provides great advantages. IBTs provide a much more convenient way of including the body motion and deformation by using a stationary non-deforming Cartesian grid. While these methods simplify the grid generation process, a detailed mathematical understanding of the IBT is necessary to avoid a negative impact of the boundary treatment on the robustness, the convergence behavior and the accuracy of the numerical scheme.

Immersed boundary methods also possess well known shortcomings. Most IBTs are only lower-order accurate and suffer from robustness issues when extended to higher-order. High accuracy near the wall is, however, required when simulating laminar to turbulent transition scenarios for wall bounded flows to capture the relevant instability mechanisms. Moreover, for high Reynolds number viscous flow simulations, current immersed boundary approaches are inefficient in resolving the viscous boundary layers since the Cartesian mesh layout generally does not allow the use of (wall-normal) high aspect ratio cells in the vicinity of the wall. This issue has been addressed in several research investigations, but the current approaches, mainly based on the application of wall-functions near the immersed boundary, lack maturity and require further research.

The proposed immersed boundary approach for the compressible Navier–Stokes equations, presented in this paper is an extension of the Immersed Interface Method (IIM) initially developed by Brehm and Fasel [16,17] for the incompressible Navier–Stokes equations, and Ito [18], we use the expression for the local truncation error to derive a set of linear equations for the coefficients of the boundary stencil. In addition to this set of linear equations, a supplementary equation based on stability considerations at the irregular grid point is used. In this paper, an irregular grid point is present when a regular (interior) grid stencil crosses the computational (fluid/solid) boundary or an interface separating two regions with different material properties. Various other higher-order accurate immersed boundary methods appeared recently in the literature, such as the higher-order cut cell method by Duan et al. [10], the higher-order ghost-cell immersed boundary method for solving the linearized perturbed compressible equations by Seo and Mittal [19], and the compact Finite-Difference (FD) based immersed boundary method by Linnick and Fasel [6] developed for solving the incompressible Navier–Stokes equations in stream function-vorticity formulation. The inclusion of local stability considerations is what distinguishes our approach from other IBT approaches discussed in the literature. These IBTs are commonly derived solely based on considering the accuracy of the numerical scheme. The importance of incorporating local stability considerations at irregular finite-difference stencils was demonstrated in Brehm and Fasel [20] by conducting a stability analysis of a higher-order accurate immersed boundary method based on compact finite-differences developed by Linnick and Fasel [6]. It was concluded that the numerical scheme is only conditionally stable for cell Reynolds numbers less than a limiting value that depends upon the location of the immersed boundary. The conditional stability of this scheme may cause robustness issues at least for non-expert users. Our method has been shown to be high-order accurate and extremely robust even for problems including moving or deforming boundaries. In Brehm and Fasel [21], the incompressible Navier–Stokes solver was coupled with a finite element solver in order to investigate the fluid structure interaction (FSI) of a flow past a flexible filament.

In the present paper an extension of our IIM for the compressible Navier–Stokes equations is discussed. The paper is organized as follows: The first part of the paper provides an overview of the numerical methods for the interior scheme.

In the following section, the numerics of the immersed boundary scheme for the convective and viscous terms of the compressible Navier–Stokes equations are discussed. The truncation error convergence properties of the numerical scheme are analyzed by applying the method of manufactured solutions. An extensive stability analysis of the numerical scheme for the Euler equations demonstrates the superior stability characteristics of the current approach. The stability property of the current scheme is also compared to other IBTs. For validation purposes, the current approach is applied to various canonical test problems including subsonic flows past a cylinder and a sphere. In the last part of the paper, the immersed boundary method is used to study the downstream development of a second mode instability wave in a Mach 6 boundary layer on a flat plate with and without a porous wall as well as simulating the effect of a discrete three-dimensional spherical roughness element placed in a subsonic boundary layer flow.

## 2. Numerical methods

### 2.1. Space and time discretization of the interior scheme

The compressible Navier–Stokes equations considering an ideal, Newtonian, non-reactive gas written in vector form are

$$\frac{\partial \mathbf{W}}{\partial t} + \nabla \cdot (\vec{\mathcal{F}} - \vec{\mathcal{F}}_v) = 0, \quad \text{with } \vec{\mathcal{F}} = (\mathbf{F}^1, \mathbf{F}^2, \mathbf{F}^3) \quad \text{and} \quad \vec{\mathcal{F}}_v = (\mathbf{F}_v^1, \mathbf{F}_v^2, \mathbf{F}_v^3). \quad (1)$$

The conservative variable vector  $\mathbf{W} = (\rho, \rho u, \rho v, \rho w, \rho H - p)^T$  and the inviscid fluxes are

$$\mathbf{F}^1 = \begin{bmatrix} \rho u \\ \rho u^2 + p \\ \rho uv \\ \rho uw \\ \rho uH \end{bmatrix}, \quad \mathbf{F}^2 = \begin{bmatrix} \rho v \\ \rho vu \\ \rho v^2 + p \\ \rho vw \\ \rho vH \end{bmatrix}, \quad \text{and} \quad \mathbf{F}^3 = \begin{bmatrix} \rho w \\ \rho wu \\ \rho wv \\ \rho w^2 + p \\ \rho wH \end{bmatrix},$$

where the total enthalpy is  $H = h + \mathbf{u} \cdot \mathbf{u}/2$  with  $h = \gamma RT/(\gamma - 1)$  and the ideal gas law  $p = \rho RT$  is used. The viscous fluxes are

$$\mathbf{F}_v^1 = \begin{bmatrix} 0 \\ \tau_{xx} \\ \tau_{xy} \\ \tau_{xz} \\ f_v^1 \end{bmatrix}, \quad \mathbf{F}_v^2 = \begin{bmatrix} 0 \\ \tau_{yx} \\ \tau_{yy} \\ \tau_{yz} \\ f_v^2 \end{bmatrix}, \quad \text{and} \quad \mathbf{F}_v^3 = \begin{bmatrix} 0 \\ \tau_{zx} \\ \tau_{zy} \\ \tau_{zz} \\ f_v^3 \end{bmatrix},$$

where  $f_v^i = u_j \tau_{ij} - q_i$  with  $q_i = -\kappa \partial T / \partial x_i$ . In the above equations  $\rho$  is the density,  $\mathbf{u} = [u, v, w]$  is the velocity vector,  $p$  is the static pressure,  $T$  is the temperature,  $\gamma$  is the specific heat ratio,  $R$  is the gas constant, and  $\kappa$  is the thermal conductivity. The viscous stress tensor is

$$\tau_{ij} = \mu \left( \frac{\partial u_i}{\partial x_j} + \frac{\partial u_j}{\partial x_i} \right) + \delta_{ij} \lambda \frac{\partial u_k}{\partial x_k}, \quad (2)$$

where  $\lambda = -\frac{2}{3}\mu$  is the second viscosity, the dynamic viscosity is given by  $\mu$ , and  $\delta_{ij}$  is the unit tensor.

The interior discretization of the convective terms follows the approach presented in Laible and Fasel [22]. The forward-flux,  $\mathbf{F}^+$ , and the backward-flux,  $\mathbf{F}^-$ , are discretized with  $n$ th-order accurate upwind-biased finite-differences using centered grid stencils as proposed by Zhong [23]. As in Laible and Fasel [22], a parameter  $\alpha$  is used to determine the degree of upwinding for the upwind-biased finite-differences

$$\frac{\partial \phi}{\partial x} \Big|_i = \sum_{k=i-n_s}^{i+n_s} c_k \phi_k - \alpha \overline{\Delta x} \frac{\partial^{2n_s-1} \phi}{\partial x^{2n_s-1}} \Big|_i, \quad (3)$$

where  $c_k$  is the  $k$ th FD stencil coefficient,  $\overline{\Delta x}$  is the averaged grid spacing over the spatial extent of the stencil and,  $n_s = (n + 1)/2$  determines the number of grid points in the stencil. The stencil coefficients for the interior scheme are derived in Appendix A. Note that a central FD stencil is obtained for  $\alpha = 0$ . In this case a higher-order filter based on the work by Visbal and Gaitonde [24] is used to stabilize the numerical solution.

In the current paper, it is assumed that the numerical fluxes are approximated with flux vector splitting schemes, i.e., Lax Friedrichs, van Leer, AUSM-family, etc. The compressible Navier–Stokes equations are advanced in time with an explicit fourth-order accurate Runge–Kutta scheme based on the Shu–Osher formulation [25]. For accurately capturing flow discontinuities higher-order shock capturing schemes [26] are also available. The computational domain is decomposed into block-structured sub-domains supporting adaptive-mesh refinement as well as generalized curvilinear coordinates. In order to maintain higher-order accuracy across coarse-fine block interfaces, up-to fourth-order accurate prolongation and restriction operators are used. On curvilinear meshes, free-stream conservation is obtained by computing the metric terms in

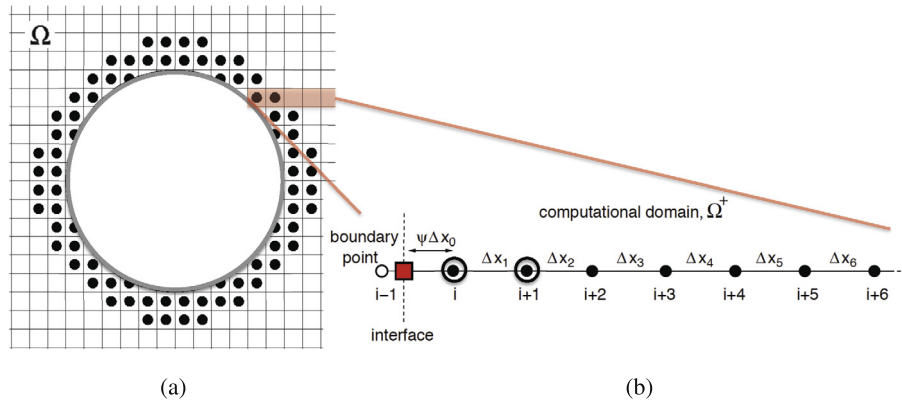


**Fig. 2.** (a) Localization illustrated in 2D for circle immersed into Cartesian grid. (b) Computational setup in the vicinity of the immersed boundary including irregular grid points (○), point in fluid (●) and point in solid (dropped) (○) the computational domain, and a boundary point (□).

strong conservation form. In Nonomura et al. [27], it has been noted that free-stream conservation is achieved when employing the same difference operators for the spatial discretization as well as for the discretization of the metric terms in strong conservation form. The discretization of the viscous terms is available in conservative form as presented in Eq. (1) and in non-conservative form. In non-conservative form, all spatial derivatives are carried through. Thus, the second derivatives and cross derivatives with respect to primitive variables are directly computed, such as,

$$\frac{\partial (\tau_{xy})}{\partial y} = \frac{d\mu}{dT} \frac{\partial T}{\partial y} \left( \frac{\partial u}{\partial y} + \frac{\partial v}{\partial x} \right) + \mu \left( \frac{\partial^2 u}{\partial y^2} + \frac{\partial^2 v}{\partial y \partial x} \right). \quad (4)$$

The derivative of the dynamic viscosity is simply obtained by differentiating Sutherland's law. It has been observed that successively applying two first-order derivative operators may induce numerical instabilities. Indeed, it can be shown that applying a first difference operator twice instead of directly computing the second derivative leads to a pair of decoupled discrete operators, which can lead to odd–even decoupling promoting numerical instabilities. Applying filters after each time-step (or Runge–Kutta sub-step) suppresses these modes. Careful studies by Visbal and Gaitonde [24] provide strong evidence that this instability can be successfully suppressed by applying higher-order spatial filters. The non-conservative approach, however, is generally computationally more expensive and requires more memory, particularly in generalized curvilinear coordinates.

## 2.2. Immersed boundary method for the convective terms

In this section, the theoretical basis of the IIM presented in Brehm and Fasel [20] is extended to the compressible Navier–Stokes equations. Many immersed methods have been developed in the past; however, in the derivation of these schemes, usually only the order of accuracy of the local truncation error of the numerical scheme has been considered. *A posteriori*, the numerical stability of these schemes is commonly demonstrated (in a global sense) by considering a number of different test-problems, and in a few cases, an additional global matrix stability analysis is employed (see for example Zhong [9]). The basis of the current immersed boundary method is that the stencil coefficients are locally optimized in order to improve the stability of the scheme.

### 2.2.1. Basic concept of local stability enhancement

The notion of developing a strategy for improving the spectral properties of immersed boundary methods originated from the idea that the stability of the numerical scheme can be formulated as an  $N$ -dimensional optimization problem, where  $N$  represents the number of irregular grid points shown in Fig. 2. Instead of solely considering the local truncation error in the derivation of the FD stencil at an irregular grid point, an over-determined system of equations is constructed to determine the stencil coefficients. We employed an over-determined system of equations because it allows to select free parameters, which can be tuned towards optimizing the local stability properties of the FD stencil. Thus, assuming one free parameter per irregular grid point an  $N$ -dimensional optimization problem for  $N$  irregular grid points is obtained.

The objective function of the optimization problem must be carefully chosen and depends on the nature of the particular partial-differential equation of interest. For advection–diffusion-type equations, the spectral radius of the update matrix may be considered an appropriate objective function [20]. In the current paper, we refer to the update matrix as the matrix which updates the numerical solution from time  $t_n$  to the next time-step,  $t_{n+1}$ . The update matrix, therefore, contains information about the spatial and temporal discretization of the numerical scheme. The spectral radius is well-suited in this situation, because its actual value is associated with the stability of the numerical scheme and it can be used to formulate a necessary condition for the stability of the update matrix. Different options such as using the real eigenvalue of the spatial

discretization matrix were explored but turned out to be less suitable for formulating appropriate constraints on the stencil coefficients. For non-linear systems of equations, a linearization is necessary prior to applying the outlined linear stability analysis concepts. Note that this paper is exclusively concerned with the linear stability of the immersed boundary scheme and, therefore, neglects possible non-linear effects on the stability.

In principal, it is possible to solve a coupled  $N$ -dimensional optimization problem for  $N$  irregular grid points. From a practical point of view, however, it is not very efficient or desirable to solve such a large system of equations, especially for FSI problems where the grid topology is time dependent, thereby requiring this procedure to be repeated at each time-step. Therefore, in the current approach, we isolated the boundary stencils from the remainder of the computational domain so that the optimization problem can be formulated for each irregular grid-point separately. Instead of solving a global  $N$ -dimensional optimization problem,  $N_l \leq N$  lower dimensional optimization problems are obtained at each irregular grid point (Fig. 2). This approach greatly reduces the computational expense needed to determine the “optimal” stencil coefficients. We refer to the aspect of turning the global  $N$ -dimensional problem into  $N_l$  lower-dimensional problems as “localization” or “localization assumption”. In Brehm and Fasel [20], it was demonstrated, both numerically and analytically, that for advection–diffusion type equations, the localization assumption appears to be valid as long as the von Neumann number does not reach a limiting value. For a more detailed discussion on the original approach, see Brehm and Fasel [20].

A simple 1D advection–diffusion equation,

$$\frac{\partial \phi}{\partial t} = -c_x \frac{\partial \phi}{\partial x} + \frac{\partial}{\partial x} \left( \beta \frac{\partial \phi}{\partial x} \right), \quad (5)$$

is taken as a sample problem to outline the main steps of the approach. In Eq. (5),  $c_x$  is the advection speed and  $\beta$  is the diffusion coefficient.

As shown in Fig. 2(b), Eq. (5) is discretized over a computational domain of unit length. An irregular grid point is assumed at the left end of the computational domain with a boundary distance of  $\psi \Delta x_0$  to the neighboring grid point,  $x_i$ , and  $0 < \psi \leq 1$ . The FD stencil coefficients are derived by following the three steps listed below:

1. In order to achieve the desired accuracy of the FD stencil, the continuous convection–diffusion operator is compared to its discrete approximation. The truncation error for the convection–diffusion operator is

$$\begin{aligned} \tau_i = & \left( -u \frac{\partial \phi}{\partial x} + \frac{\partial}{\partial x} \left( \beta \frac{\partial \phi}{\partial x} \right) + f \right)_{x=x_i} \\ & - \left( \hat{\phi}_{\partial \Omega} c_{\partial \Omega} + \hat{\phi}_i c_1 + \hat{\phi}_{i+1} c_2 + \hat{\phi}_{i+2} c_3 + \hat{\phi}_{i+3} c_4 + C \right), \end{aligned} \quad (6)$$

where  $c_i$  denotes the stencil coefficients,  $C$  is an additional constant containing the source term,  $f_i$ , and  $\hat{\phi}_i$  is the discrete approximation of the continuous variable,  $\phi$ . In order to achieve  $n$ th-order accuracy, only  $n + 2$  grid points are needed. However, in order to provide improved stability characteristics of the scheme, one additional grid point is added and used as a free parameter to adjust the FD stencils in the vicinity of the boundary. Furthermore, without using an additional grid point the FD stencil becomes singular for small boundary distances scaling with  $\psi^{-1}$ .

2. A key feature of this new immersed boundary method is the consideration of local stability constraints in order to stabilize the overall numerical scheme. For the derivation, the spatial discretization represented by  $\tilde{\mathbf{A}}$  is coupled with the temporal discretization. For the current approach, a simple Euler-forward time-integration will be employed, which results in the combined temporal and spatial discretization matrix,

$$\mathbf{A} = \mathbf{I} + \Delta t \tilde{\mathbf{A}}. \quad (7)$$

Formally, the combined temporal and spatial discretization matrix,  $\mathbf{A}$ , can be written as a product of two matrices

$$\mathbf{A} = \mathbf{E} \cdot \mathbf{A}_{id}. \quad (8)$$

The purpose of matrix  $\mathbf{E}$  is to project matrix  $\mathbf{A}_{id}$  onto the combined temporal and spatial discretization matrix,  $\mathbf{A}$ . In this context,  $\mathbf{A}_{id}$  represents the full discretization matrix on a uniform (or generalized curvilinear) grid without an immersed boundary. The last (or  $(n + 3)$ th) stencil coefficient (for the  $n$ th-order accurate scheme) is determined by minimizing the  $L_2$ -norm of the so-called perturbation matrix,  $\mathbf{E}$ .

3. In the last step for deriving the immersed boundary method, it must be demonstrated that for convection dominated problems, the stability of the discretization matrix can be determined locally. It is essential that the irregular stencils can be isolated from the rest of the computational domain so that their stability behavior can be adjusted locally. The validity of the localization assumption was demonstrated both numerically and analytically [20].

### 2.2.2. Extension of IIM to the compressible Navier–Stokes equations

The main difference for the application of the IIM to the compressible Navier–Stokes equations instead of the incompressible Navier–Stokes equations (solved by utilizing the approximate projection method) is the use of numerical fluxes. Flux vector splitting schemes, such as van Leer [28], Lax–Friedrichs, and AUSMPW+, are adopted here. In the flux vector splitting approach, the convective flux is divided into a forward-flux and a backward-flux,  $\mathbf{F} = \mathbf{F}^+ + \mathbf{F}^-$ . The flux vector

splitting approach is also applied at irregular grid points, which can be employed to stabilize the irregular grid stencils. Assuming subsonic flow speeds in the vicinity of the immersed boundary, which is generally always true for no-slip wall boundary conditions, upwinding can always be applied in the upwind direction towards the wall. This is in contrast to the scalar advection equation where the advection speed determines the upwind direction [20]. The basic ideas of the implementation are discussed for the 1D Euler equations in conservative variable formulation,

$$\begin{pmatrix} \rho \\ \rho u \\ E \end{pmatrix}_t = \begin{pmatrix} \rho u \\ \rho u^2 + p \\ u(E + p) \end{pmatrix}_x, \quad (9)$$

where the total energy can be expressed as  $E = \rho (T/((\gamma - 1)\gamma M^2) + u^2/2)$ . The fluid is assumed to be an ideal gas, which can be modeled by the equation of state,  $p = \rho RT$ . Applying the flux vector splitting approach to the 1D Euler equations leads to

$$\mathbf{W}_t = \mathbf{F}_x = \mathbf{F}_x^+ + \mathbf{F}_x^-, \quad (10)$$

where the solution vector can be written as  $\mathbf{W} = (w_1, w_2, w_3)^T = (\rho, \rho u, E)^T$ . In order to numerically analyze the 1D Euler system in Eq. (10), the flux Jacobian,  $\partial \mathbf{F} / \partial \mathbf{W}$ , is introduced,

$$\mathbf{W}_t = \frac{\partial \mathbf{F}}{\partial \mathbf{W}} \cdot \frac{\partial \mathbf{W}}{\partial x} = \frac{\partial \mathbf{F}^+}{\partial \mathbf{W}} \cdot \frac{\partial \mathbf{W}}{\partial x} + \frac{\partial \mathbf{F}^-}{\partial \mathbf{W}} \cdot \frac{\partial \mathbf{W}}{\partial x}. \quad (11)$$

This leads to an equation including the derivatives of the forward/backward-flux vectors,  $\mathbf{F}^\pm$ , with respect to the solution vector  $\mathbf{W}$ . The gradient of the convective flux vectors,  $\mathbf{F}^\pm$ , is discretized with the discrete forward difference operator,  $\mathbf{D}_x^+$  (for the forward-flux) and in backward direction with the discrete backward difference operator,  $\mathbf{D}_x^-$  (for the backward-flux),

$$\begin{aligned} \mathbf{W}_t &= \frac{\partial \mathbf{F}^+}{\partial \mathbf{W}} \cdot \frac{\partial \mathbf{W}}{\partial x} + \frac{\partial \mathbf{F}^-}{\partial \mathbf{W}} \cdot \frac{\partial \mathbf{W}}{\partial x} \\ &\cong \frac{\partial \mathbf{F}^+}{\partial \mathbf{W}} \cdot (\mathbf{D}_x^+ \cdot \mathbf{W}) + \frac{\partial \mathbf{F}^-}{\partial \mathbf{W}} \cdot (\mathbf{D}_x^- \cdot \mathbf{W}). \end{aligned} \quad (12)$$

The details regarding the structure of the forward and backward difference operators,  $\mathbf{D}_x^\pm$ , are provided below. For numerical analysis of the boundary stencils, the equations are considered in terms of the numerical error vector,  $\boldsymbol{\varepsilon}$ ,

$$\boldsymbol{\varepsilon}_t = \frac{\partial \mathbf{F}^+}{\partial \mathbf{W}} \cdot (\mathbf{D}_x^+ \cdot \boldsymbol{\varepsilon}) + \frac{\partial \mathbf{F}^-}{\partial \mathbf{W}} \cdot (\mathbf{D}_x^- \cdot \boldsymbol{\varepsilon}). \quad (13)$$

Note that for the linear numerical analysis of the scheme, it is assumed that the components of the flux Jacobians are “frozen” and independent of the solution vector. Moreover, by assuming linear boundary conditions it can be readily recognized that homogeneous boundary conditions can be applied to the error vector.

The interior discretization of the governing equations was discussed in Section 2.1. The forward-flux difference,  $\mathbf{F}_x^+$ , and the backward-flux difference,  $\mathbf{F}_x^-$ , are discretized with an  $n$ th-order accurate upwind-biased FD scheme as proposed by Zhong [23]. Depending on the order-of-accuracy  $\mathcal{O}(\Delta x^n)$  of the interior scheme  $(n + 1)/2$  irregular grid points are present assuming  $n > 1$  is an odd, positive integer. Due to the flux vector splitting approach, only one of the spatial (forward or backward) discretization matrices ( $\mathbf{D}_x^+$  or  $\mathbf{D}_x^-$ ) requires a special boundary treatment to avoid a local numerical instability. Fig. 2(b) portrays the grid points in the vicinity of an immersed boundary. For the setup displayed in Fig. 2(b), a stable discretization of the first derivative of the backward-flux vector,  $\mathbf{F}_x^-$ , at the irregular grid points can simply be achieved by considering more grid points from the right (backward) side than from the left (forward) side. The FD stencil for the first derivative of the backward-flux vector,  $\mathbf{F}_x^-$ , can be formally written as

$$\left. \frac{\partial \phi}{\partial x} \right|_k = c_{\partial \Omega} \phi_{\partial \Omega} + \sum_{m=1}^{p_k+1} c_{i+m-1} \phi_{i+m-1}, \quad (14)$$

where  $p_k$  is the local order-of-accuracy at grid point  $x_k$ ,  $k$  is the grid index of the irregular grid point,  $k \in \{i, i + 1, \dots\}$ ,  $\phi_{\partial \Omega}$  is the boundary condition at the grid line intersection point, and the FD stencil at  $x = x_k$  contains  $n_k = p_k + 2$  grid points. The stencil coefficients are determined by applying the weighted least-squares procedure. Note that in the weighted least-squares procedure all weights are set to one except the weight of the grid point closest to the immersed boundary which is set to the non-dimensional boundary distance,  $\psi$ . The type of FD discretization in Eq. (14) takes advantage of the eigenvalue structure of the Jacobian of  $\mathbf{F}_x^-$ . It is typically referred to as biased FD stencil, where grid points on the side of the incoming characteristic are weighted more strongly to produce a stable numerical scheme.

To obtain a stable FD discretization of the first derivative of the forward-flux vector,  $\mathbf{F}_x^+$ , at irregular points an optimization procedure is employed. To illustrate the optimization procedure (discussed in Section 2.2.3), we consider a third-order accurate immersed boundary treatment. Two types of irregular FD stencils are generally used, where only one of them uses the boundary conditions applied at the grid line intersection points. For example, for a fifth-order accurate interior discretization we obtain three irregular grid points,  $x_i$ ,  $x_{i+1}$ , and  $x_{i+2}$ . Utilizing a third-order accurate immersed boundary



scheme, only the irregular FD stencils at  $x_i$  and  $x_{i+1}$  will use the boundary conditions. For higher-order accuracy, additional irregular FD stencils are necessary (see also [Appendix C](#)). The irregular FD stencils at  $x_k$  with  $k \in \{i, i+1\}$  use  $p_k + 2$  grid points to achieve a  $p_k$ th-order accurate approximation of the gradients. Note that for a  $p_k$ th-order accurate first derivative only  $p_k + 1$  grid points are strictly needed. The additional stencil coefficient is used as a free parameter in the optimization procedure in Section 2.2.3. Depending on the stencil width (or order-of-accuracy) of the interior FD scheme additional irregular grid points are present. As mentioned above, these FD stencils are the second kind of irregular FD stencils for  $\mathbf{F}_x^+$ . These stencils do not use the boundary conditions and, therefore, do not involve a free parameter. The FD approximations for the gradients of the forward-flux vector,  $\mathbf{F}_x^+$ , at these irregular grid points  $x_k$  with  $k \in \{i+2, i+3, \dots\}$  are evaluated by considering  $n_L = k - i$  grid points to the left of  $x_k$  and  $n_L - 1$  grid points to the right of  $x_k$ . This setup allows the FD stencils to be biased towards the left side, and the order of the FD stencil is  $2n_L - 1$ .

The basic steps as outlined in Section 2.2.1 are applied to derive the stencil coefficients of the irregular FD stencils at  $x_i$  and  $x_{i+1}$ . The derivation of the stencil coefficients is discussed for the gradient of the convective terms of the compressible Navier–Stokes equations at  $x_{i+1}$ . The approach to derive the irregular FD stencil coefficients at  $x_i$  is identical and it is, therefore, omitted for the sake of brevity. To achieve a third-order accurate discretization of the first derivative at  $x_{i+1}$ , the stencil coefficients need to fulfill the following system of equations:

$$\begin{pmatrix} 1 & 1 & 1 & 1 \\ \Delta x_{\partial\Omega} & \Delta x_i & 0 & \Delta x_{i+2} \\ \frac{\Delta x_{\partial\Omega}^2}{2!} & \frac{\Delta x_i^2}{2!} & 0 & \frac{\Delta x_{i+2}^2}{2!} \\ \frac{\Delta x_{\partial\Omega}^3}{3!} & \frac{\Delta x_i^3}{3!} & 0 & \frac{\Delta x_{i+2}^3}{3!} \end{pmatrix} \cdot \begin{pmatrix} c_{\partial\Omega} \\ c_i \\ c_{i+1} \\ c_{i+2} \end{pmatrix} = \begin{pmatrix} 0 \\ 1 \\ 0 \\ 0 \end{pmatrix} + c_{i+3} \begin{pmatrix} -1 \\ -\Delta x_{i+3} \\ -\frac{\Delta x_{i+3}^2}{2!} \\ -\frac{\Delta x_{i+3}^3}{3!} \end{pmatrix}, \quad (15)$$

where  $\Delta x_k = x_k - x_{i+1}$  with  $k \in \{\partial\Omega, i, i+1, i+2, i+3\}$ , and  $c_{\partial\Omega}$  denotes the stencil coefficient of the boundary point. The original immersed boundary method discussed in Brehm and Fasel [20] was applied to a simple convection–diffusion equation. In contrast to the original approach [20], when applying the immersed boundary method to the compressible Navier–Stokes equations the coupling between the continuity, momentum, and energy equations needs to be considered. In the present approach for compressible flows, all components of the flux vector use the same FD stencil coefficients. To determine the free stencil coefficient,  $c_{i+3}$ , in Eq. (15), the fully coupled system of partial differential equations is considered. In semi-discrete form, the basic structure of the spatial discretization matrix,  $\tilde{\mathbf{A}}$ , can be written as

$$\begin{pmatrix} \mathbf{e}_1 \\ \mathbf{e}_2 \\ \mathbf{e}_3 \end{pmatrix}_t + \underbrace{\frac{\partial \mathbf{F}^+}{\partial \mathbf{W}} \otimes \begin{pmatrix} \mathbf{D}_x^+ & \mathbf{D}_x^+ & \mathbf{D}_x^+ \\ \mathbf{D}_x^+ & \mathbf{D}_x^+ & \mathbf{D}_x^+ \\ \mathbf{D}_x^+ & \mathbf{D}_x^+ & \mathbf{D}_x^+ \end{pmatrix}}_{\tilde{\mathbf{A}}} \cdot \begin{pmatrix} \mathbf{e}_1 \\ \mathbf{e}_2 \\ \mathbf{e}_3 \end{pmatrix} = 0, \quad (16)$$

where  $\mathbf{D}_x^+$  contains the FD coefficients at regular grid points derived in [Appendix A](#) and irregular grid points as shown in Eq. (15). The error in the continuity, momentum and energy equations are denoted by  $\mathbf{e}_1, \mathbf{e}_2, \mathbf{e}_3$ . The flux Jacobian  $\partial \mathbf{F}^+ / \partial \mathbf{W}$  in Eq. (16) is evaluated locally at the location of the irregular grid point.

### 2.2.3. Optimization problem for IIM stencil coefficients

Similar to the derivation in Brehm and Fasel [20], the Euler-forward time-integrator is used to introduce the coupling between the temporal and spatial discretizations, which then leads to the full discretization matrix,  $\mathbf{A}$ , shown in Eq. (7). The free stencil coefficients are then determined by minimizing the  $L_2$ -norm of the perturbation matrix,  $\mathbf{E}$ , in Eq. (8) which isolates the effect of the immersed boundary from the full discretization matrix,  $\mathbf{A}$ . Note that for the ideal discretization matrix,  $\mathbf{A}_{id}$ , it is assumed that the computational domain continuously extends by the half-width of the interior stencil (the grid point closest to the immersed boundary outside of the computational domain in [Fig. 2](#)).

The optimization procedure for the stencil coefficients of the FD operators applied to the differentiation of the forward fluxes at the irregular points  $x_i$  and  $x_{i+1}$  is discussed next. For the higher-order accurate immersed boundary treatment, the optimization procedure of the boundary stencil requires generally  $(n+1)/2$  free parameters, where  $(n+1)/2$  is equal to the number of irregular grid points and  $n > 1$  is the order of the interior (or regular) scheme. In the current third-order accurate example, two free parameters are used in the discretization matrix, where the first parameter is related to the discretization of the forward-flux gradient at  $x_{i+1}$ , and the second coefficient is related to the forward-flux gradient at  $x_i$ . To avoid a 2D optimization problem based on these two parameters, a strategy is pursued where two 1D optimization problems are solved sequentially. The first free parameter for the FD stencil at  $x_{i+1}$  is determined by using an FD discretization at  $x_i$ , which is equal to the discretization of the ideal scheme. Thus, the perturbation due to the discretization of the gradient at  $x_i$  does not affect the first optimization problem, which is used to determine the FD stencil at  $x_{i+1}$ . In the second 1D optimization problem, the previously determined FD stencil coefficients at  $x_{i+1}$  are taken from the solution of the first optimization problem, and only the free parameter associated with the FD stencil at  $x_i$  is determined by minimizing the  $L_2$ -norm of the perturbation matrix  $\mathbf{E}$ . For the results presented here, no iterative procedure was used to fine-tune the two parameters obtained from the two 1D optimization problems. Our numerical experiments indicate that solving

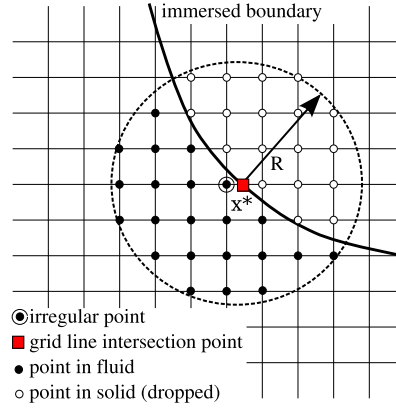


**Fig. 3.** Schematic of candidate points in the vicinity of an irregular grid point considered in the pressure/temperature extrapolation stencil.

two 1D problems sequentially is sufficient to achieve a stable discretization in the vicinity of the immersed boundary. To determine the grid stencil coefficients, a sub-matrix with dimension  $(N_{loc} \times N_{loc})$ , of the full spatial discretization matrix,  $\tilde{\mathbf{A}}$ , is employed. When the localization assumption applies, only a small number of grid points,  $N_{loc}$ , in the vicinity of the irregular stencil can be considered for the optimization problem, and a globally stable FD discretization can be achieved.  $N_{loc}$  is typically equal to the width of the largest irregular FD stencil plus one. [Appendix B](#) provides additional details about the optimization procedure and discusses some aspects regarding the computational efficiency of this approach. In addition, [Appendix C](#) presents a brief summary of the immersed boundary method for the convective terms.

#### 2.2.4. Imposition of pressure and temperature boundary conditions

One important aspect of the present immersed boundary method for the convection terms of the compressible Navier–Stokes equations has not yet been addressed. In order to compute flux derivatives it is assumed that the fluxes are known at the immersed boundary. For no-slip wall boundary conditions the velocities are set to zero at the wall. As it is common practice for numerical solutions of the Navier–Stokes equations, we apply Neumann boundary conditions to the pressure field. Based on the solid surface and flow conditions, Dirichlet or Neumann boundary conditions are used for the temperature field. The extrapolation procedure for pressure and temperature boundary conditions has a strong effect on the accuracy and stability of the numerical scheme. Commonly used weighted least-squares approaches, here referred to as WLSQR, have the disadvantage that they can become ill-conditioned when considering a large stencil size, particularly in 3D. The WLSQR method has some similarities to the method in Seo and Mittal [19] and Luo et al. [29]; however, we use a different weight function in the present work. Furthermore, for the current immersed boundary method, we also use a rank-based stencil selection approach where we are able to select the minimum number of grid points,  $n_{min}$ , necessary to obtain the desired order of accuracy.

For any candidate grid point, the stencil search algorithm checks if the matrix, which has to be inverted to obtain the stencil extrapolation coefficients, retains full rank. This check is based on ensuring that the smallest singular value of this matrix is greater than zero and the matrix, therefore, remains non-singular. A schematic of the candidate points considered for the extrapolation stencils is provided in [Fig. 3](#). The scheme searches for candidate points within a circle/sphere of radius,  $R$ , centered around the grid line intersection point,  $\mathbf{x}^*$ . The candidate points are sorted by their respective distance to the grid line intersection point. A grid point is added if matrix,  $\mathbf{M}_E$ , has full rank when including this point.

Each row of  $\mathbf{M}_E$  contains a row vector of the form

$$\mathbf{r}_k = [1, \Delta x_k^*, \Delta y_k^*, \Delta z_k^*, (\Delta x_k^*)^2, (\Delta y_k^*)^2, (\Delta z_k^*)^2, \Delta x_k^* \Delta y_k^*, \Delta x_k^* \Delta z_k^*, \Delta y_k^* \Delta z_k^*, \text{h.o.t.}]^T, \quad (17)$$

where  $\Delta \mathbf{x}_k^* = \mathbf{x}_{i_k, j_k, k_k} - \mathbf{x}^*$ ,  $\mathbf{x}^* = [x^*, y^*, z^*]$  is the location of the grid line intersection point and  $x_{i_k, j_k, k_k}$  is the location of the  $k$ th grid point added to matrix  $\mathbf{M}_E$ . The extrapolation approach with rank based stencil selection is referred to as WLSQR+.

The extrapolation coefficients are obtained by solving the following minimization problem for the unknown boundary value  $\phi^*$ :

$$\left( \sum_{k=1}^{n_R + n_A} w_k (\Delta \phi_{i_k, j_k, k_k}^*)^2 \right) \rightarrow \min, \quad (18)$$

where the  $n_R = n_{min}$  grid points were chosen based on the rank-based stencil selection search and  $n_A$  additional grid points were added to form an over-determined system of equations. The weights,  $w_k$ , are chosen in the form

$$w_k = \frac{1}{((\Delta x_k^*)^2 + (\Delta y_k^*)^2 + (\Delta z_k^*)^2)^{p/2}}, \text{ commonly with } p/2 \geq 0. \quad (19)$$





where  $k \in \{i, i+1, \dots\}$ . A multi-dimensional FD stencil is needed for computing cross-derivatives. The  $xy$ -derivative is shown in Eq. (24) as an example of a cross-derivative,

$$\left. \frac{\partial^2 \phi}{\partial x \partial y} \right|_{i,j,k} = c_{\partial\Omega} \phi_{\partial\Omega} + \sum_{m=1}^{n_R-1+n_A} c_{i_m, j_m, k_m} \phi_{i_m, j_m, k_m}. \quad (24)$$

With the rank based stencil selection approach outlined in Section 2.2.4,  $n_R = n_{\min}$  grid points (including the boundary point) are chosen for the stencil computation. Additional  $n_A$  grid points are added to form an over-determined system of equations. The contribution from the boundary point  $\phi_{\partial\Omega}$  is chosen at a grid line intersection with the immersed geometry. For irregular grid points which are irregular with respect to several directions (see Fig. 4), we choose the intersection point with the larger boundary distance ( $\max(\psi_x, \psi_y)$ ).

### 3. Truncation error study

The Method of Manufactured Solutions (MMS) is used to verify the formal order-of-accuracy of the convective and viscous terms with and without immersed boundary in 2D and 3D. For the truncation error study of the viscous terms, the viscosity is set to  $\mu = 1$  to ensure dominance of the viscous terms over the convection terms. Different options for the extrapolation of the pressure and temperature boundary conditions (see Section 2.2.4) and their impact on the accuracy of the overall numerical scheme are explored in Appendix D. The truncation error is computed as the difference between a reference solution and the numerical approximations of the convection (inviscid) and the combined convection and diffusion terms (viscous) of the Navier–Stokes equations (1) for one right-hand-side evaluation. The truncation error is computed for the continuity equation, the momentum equations and the energy equation. It has been observed, however, that the  $L_2$  and  $L_\infty$  error norms for the different equations behave similarly. Hence, only the results for the truncation error of the  $x$ -momentum equation are presented. The reference solution is obtained with a sixth-order accurate centered FD scheme on a highly resolved mesh. For the truncation error studies, the flow field is initialized with the following thermodynamic state,

$$\begin{aligned} p(x, y, z) &= \frac{1}{2} + r^2 - 2R_0 r, \text{ and} \\ T(x, y, z) &= \frac{1}{2} + r^2 - 2R_0 r, \end{aligned} \quad (25)$$

where  $R_0$  is the cylinder/sphere radius,  $r = \sqrt{(x - x_0)^2 + (y - y_0)^2 + (z - z_0)^2}$  is the local radius and  $x_0, y_0$  and  $z_0$  denote the center of the cylinder/sphere in physical coordinates. The thermodynamic state was chosen such that the pressure and temperature fields fulfill Neumann BCs at the immersed boundary. The velocity field,

$$\begin{aligned} u_{2D}(x, y) &= \cos(2\pi x) \sin(2\pi y), \\ v_{2D}(x, y) &= -\sin(2\pi x) \cos(2\pi y), \\ u_{3D}(x, y, z) &= u_{2D}(x, y) \sin(2\pi z), \\ v_{3D}(x, y, z) &= -v_{2D}(x, y) \sin(2\pi z), \text{ and} \\ w_{3D}(x, y, z) &= -2 \sin(2\pi x) \sin(2\pi y) \cos(2\pi z), \end{aligned} \quad (26)$$

is initialized to be divergence free ( $\nabla \cdot \vec{u} = 0$ ) in order to analytically satisfy the continuity equation in the incompressible limit. For the present study the computational domain is chosen to have unit length in all coordinate directions and the radius and the center of the cylinder/sphere are  $R_0 = 0.2$  and  $(x_0, y_0, z_0) = (0.5, 0.5, 0.5)$ , respectively. For the interior scheme, the fifth-order accurate upwind biased FD scheme is utilized for the convective terms. An error convergence study was carried out to confirm the expected fifth-order accuracy in the inviscid limit on uniform, stretched and wavy grids (see Appendix E). The two viscous schemes presented in Section 2.1 were implemented as formally (even)  $(2n)$ th-order accurate schemes (here,  $n = 2$ ). For the particular solution given in Eqs. (25) and (26), the error convergence study (not shown here) indicate that the non-conservative scheme is slightly more accurate compared to the conservative scheme.

The truncation error convergence plots for the inviscid case with immersed boundary treatment are shown in Fig. 5. For the results displayed in Figs. 5(a) and 5(b), the exact boundary conditions are prescribed. The results confirm that second-order and third-order convergence rates are obtained in the  $L_\infty$ -norm. For the results in Fig. 5(c), the pressure and temperature boundary condition extrapolation procedure was utilized. On a uniform grid, the truncation error convergence plots exhibit non-monotone behavior but on average second-order convergence is recovered. This non-monotone behavior disappears when grid stretching ( $\beta = 2$  in Appendix E) is employed.

Next, we studied the convergence behaviors of the truncation error for the viscous terms. The results utilizing the exact boundary conditions are provided in Figs. 6(a) and 6(b). Similar to the inviscid case the results show that the desired second and third-order convergence rates are obtained in  $L_\infty$ -norm. In all truncation error studies (BC extrapolation, inviscid, and viscous) it was observed that the third-order accurate immersed boundary method is significantly more accurate compared to the second-order scheme.

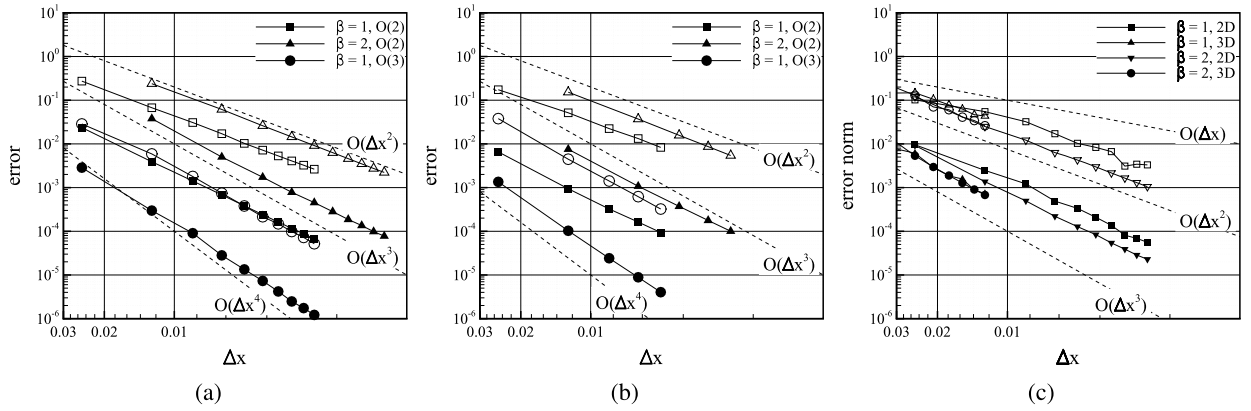


**Fig. 5.** Truncation error convergence study of convection terms using  $L_\infty$ -norm ( $\square, \circ, \triangle, \nabla$ ) and  $L_2$ -norm ( $\blacksquare, \bullet, \blacktriangle, \blacktriangledown$ ): Immersed boundary schemes with second-order and third-order accuracy using exact boundary conditions for (a) 2D, and (b) 3D test case and (c) second-order accurate scheme with boundary condition extrapolation.

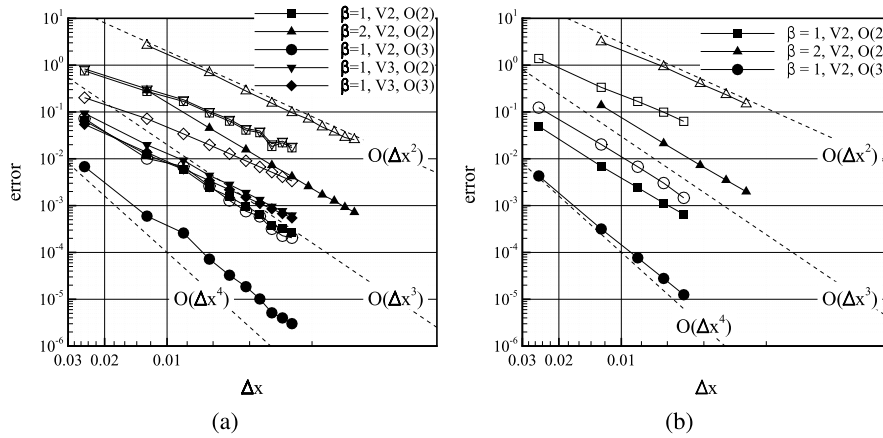


**Fig. 6.** Truncation error convergence of viscous terms using  $L_\infty$ -norm ( $\square, \circ, \triangle, \nabla, \diamond$ ) and  $L_2$ -norm ( $\blacksquare, \bullet, \blacktriangle, \blacktriangledown, \blacklozenge$ ): Immersed boundary schemes with second-order and third-order accuracy using exact boundary conditions for (a) 2D, and (b) 3D test case (V2 = conservative formulation, V3 = non-conservative formulation).

#### 4. Stability analysis

The stability of the immersed boundary method is studied by linearizing the convective terms and conducting a matrix stability analysis. The stability properties of the convective term of the spatial discretization matrix,  $\tilde{\mathbf{A}}$ , and the spatial and temporal coupled discretization matrix,  $\mathbf{A}$ , are analyzed. The standard fourth-order accurate Runge–Kutta scheme was used as time-integrator for the stability analysis of  $\mathbf{A}$ .

$$\mathbf{A} = \mathbf{I} + \Delta t \tilde{\mathbf{A}} + \frac{\Delta t^2}{2!} \tilde{\mathbf{A}}^2 + \frac{\Delta t^3}{3!} \tilde{\mathbf{A}}^3 + \frac{\Delta t^4}{4!} \tilde{\mathbf{A}}^4 \quad (27)$$

Matrix  $\mathbf{A}$  in Eq. (27) is also referred to as the update matrix updating the numerical solution from time step  $t^n$  to the next time step  $t^{n+1} = t^n + \Delta t$ .

##### 4.1. One dimensional stability analysis of the spatial discretization operator

For the 1D stability analysis, we use the  $M = 6$  boundary layer flow conditions shown in Fig. B.22 and the same domain size as for the stencil optimization procedure in Appendix B. The linear stability analysis in this section is based on the well-known Lax–Richtmyer equivalence theorem ensuring convergence by consistency and Lax-stability of the equations in semi-discretized form. The Euler equations are linearized about the mean flow field to obtain the equations in perturbation form, which we also refer to as error equation (see also Eq. (13) in Section 2.2.2). The error equation is assumed to be homogeneous and can be written in semi-discrete form as

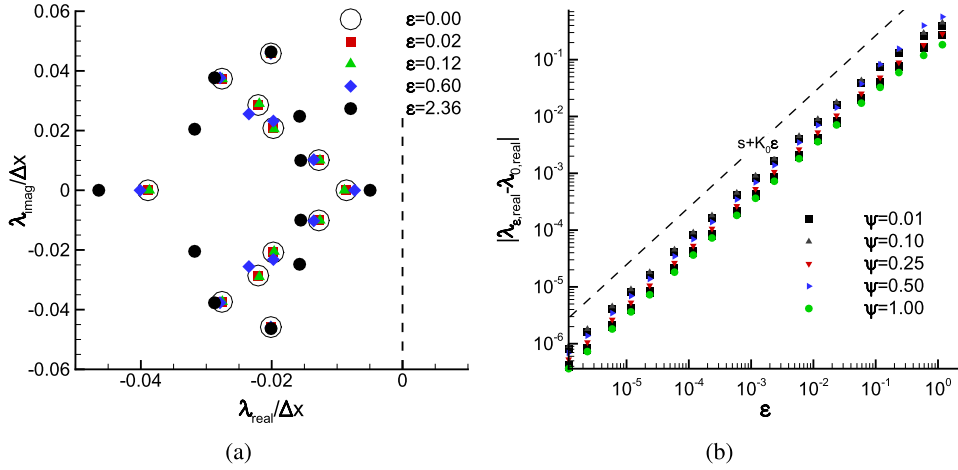


Fig. 7. (a) Close-up of pseudo-eigenvalue spectra for  $\psi = 0.01$  and (b)  $|\max(\lambda_{\epsilon, \text{real}}) - \max(\lambda_{0, \text{real}})|$  for different boundary distances.

$$\frac{d\epsilon}{dt} = -\frac{1}{\Delta x} \tilde{\mathbf{A}} \epsilon, \quad \text{with BC: } \epsilon_0(t) = 0, \quad \text{and IC: } \epsilon(t) = f(x_i). \quad (28)$$

It is assumed that  $\tilde{\mathbf{B}}$  is the identity matrix since in the current implementation we are solely concerned with explicit finite-differences. Matrix  $\tilde{\mathbf{B}}$  takes on a different form for compact FD schemes. The general solution for the linear system of ordinary differential equations with constant coefficients in terms of the independent variable  $t$  is

$$\epsilon(t) = \mathbf{C} \exp(\mathbf{N}_{\Delta x} t) \mathbf{C}^{-1} \epsilon(0), \quad (29)$$

where  $\mathbf{N}_{\Delta x}$  is the Jordan normal form of  $(-\frac{1}{\Delta x} \tilde{\mathbf{B}}^{-1} \tilde{\mathbf{A}})$  and  $\mathbf{C}$  is the transformation matrix. Numerical stability is ensured if the general solution to Eq. (28) can be bounded by a constant which is a function of time

$$\|\mathbf{C} \exp(\mathbf{N}_{\Delta x} t) \mathbf{C}^{-1}\| \leq K(t) \quad \forall t \geq 0, \quad (30)$$

where  $\|\cdot\|$  is a consistent matrix norm. Due to the non-orthogonal nature of the spatial discretization matrix with irregular FD stencils the transformation matrix is not unitary and a sufficient condition for stability cannot be easily formulated. The stability properties of the immersed boundary method are studied considering the  $\epsilon$ -pseudo-eigenvalue spectrum of the spatial discretization matrix. Lax-stability is required to ensure convergence on a finite time interval for  $\Delta x \rightarrow 0$ . The term  $\exp(\mathbf{N}_{\Delta x} t)$  in Eq. (30) must be uniformly bounded for a fixed number of grid points in a finite time-interval for Lax stability. When the real part of the eigenvalue of  $\tilde{\mathbf{A}}$ ,  $\lambda$ , is less or equal to zero and the algebraic multiplicity is equal to one, asymptotic stability is ensured. The generalized eigenvalue problem,

$$\left( \tilde{\mathbf{B}} \lambda_{\epsilon} + \frac{1}{\Delta x} \tilde{\mathbf{A}} - \mathbf{A} \mathbf{D} \right) \mathbf{v} = 0, \quad (31)$$

is solved for the  $\epsilon$ -pseudo-eigenvalue spectrum of the spatial discretization matrix. In Eq. (31), the disturbance matrix  $\mathbf{D}$  is a randomized matrix with  $\|\mathbf{D}\| = \epsilon$ . To make the solution to Eq. (31) practically tractable we only solved the generalized eigenvalue problem for a finite number (three realizations) of  $\mathbf{D}$ . This is clearly a simplification because theoretically the complete pseudo-eigenvalue spectra are the union of all eigenvalues of Eq. (31) for all possible  $\mathbf{D}$ . Furthermore, only a finite number of grid resolutions ( $N = 31, 61$ , and  $121$ ) were used in this study. The above assumptions are commonly used and consistent with the stability analysis presented in Adams and Shariff [30]. Our conclusions from this stability analysis are based on the assumption that the finite number of realizations represent the union of all eigenvalues for all possible realizations. Fig. 7(a) displays a close-up of the pseudo-eigenvalue spectrum for one of the three realizations of  $\mathbf{D}$ ,  $N = 31$ , different values of  $\epsilon$  and  $\psi = 0.01$ . The eigenvalue structures for the two other realizations and additional grid resolutions are similar (slightly perturbed), therefore, only the eigenvalues of the first realization and  $N = 31$  are shown in Fig. 7(a).

The close-up region of the  $\epsilon$ -pseudo-eigenvalue spectrum was chosen to visualize the least stable eigenvalues. Stable mildly damped solutions are obtained because all eigenvalues,  $\lambda_{\epsilon}$ , are contained within the left half plane. The dependence of  $|\max(\lambda_{\epsilon, \text{real}}) - \max(\lambda_{0, \text{real}})|$  on different values of  $\epsilon$  for three realizations of  $\mathbf{D}$  is displayed in Fig. 7(b). Note that only for  $\psi = 0.01$ , results considering all three different realizations of  $\mathbf{D}$  are shown. The condition,

$$\lambda_{\epsilon, \text{real}} \leq s + K_0 \epsilon \quad \forall \epsilon \geq 0, \quad (32)$$

has to be fulfilled to ensure algebraic stability of the full discretization for locally-stable, one-step methods. For suitable values of  $s$  and  $K_0$  in Eq. (32) each graph is bounded from above by a relationship in the form  $s + K_0 \epsilon$ . The stability analysis results for  $\epsilon = 0$  in Fig. 7(a) indicate asymptotic stability or numerical stability for long time-integration.



$$\rho(\underline{\mathbf{A}}) \leq 1. \quad (33)$$

Furthermore, the stability of the FD method is ensured if the discretization matrix,  $\underline{\mathbf{A}}$ , satisfies

$$|\underline{\mathbf{A}}| \leq 1 + C \Delta t \quad (\text{or in absence of linear source terms } |\underline{\mathbf{A}}| \leq 1), \quad (34)$$

where  $|\cdot|$  represents a consistent norm,  $C > 0$  independent of  $\Delta x$  and  $\Delta t$ . Hence, in order to further explore the stability characteristics of the immersed boundary method, the difference between  $(|\underline{\mathbf{A}}^N|_2)^{1/N}$  and the spectral radius,  $\rho(\underline{\mathbf{A}}) = |\lambda|_{\max}$ , for different values of  $\psi$  and for increasing integer values of  $N$ , is displayed in Fig. 8(b). The expression  $(|\underline{\mathbf{A}}^N|_2)^{1/N}$  converges towards the actual spectral radius of  $\underline{\mathbf{A}}$ , in accordance to Gelfand's formula [31],

$$\rho(\underline{\mathbf{A}}) = \lim_{k \rightarrow \infty} \|(\underline{\mathbf{A}})^k\|^{1/k}, \quad \forall k \in \mathbb{N}. \quad (35)$$

The linear stability of the current immersed boundary scheme is also analyzed for 2D in Appendix G.

## 5. Validation

For validation purposes the immersed boundary method is applied to simulate the flow around a cylinder and a sphere at subsonic speeds in a uniform free-stream flow for different Reynolds numbers,  $Re_D = U_\infty D / \nu$ . These 2D and 3D canonical flows are commonly used to evaluate immersed boundary methods. The flow field around a circular cylinder and a sphere are well-established test cases for IBTs for incompressible flows (Goldstein [3], Saiki [32], Calhoun [33], and Linnick [6]). A large amount of reference data is available for several Reynolds numbers.

### 5.1. Flow around a cylinder

The cylinder calculations were performed for the Reynolds numbers,  $Re = 20, 40, 100$ , and  $200$ . This Reynolds number range contains both steady and unsteady flow regimes. Experiments have shown that the well-known vortex shedding phenomena is observed at a Reynolds number of approximately 40 to 50 (see Tritton [34]). An investigation similar to the one reported in Linnick [6] was carried out here. The results were obtained with the fifth-order upwind biased FD scheme for the convective terms and a fourth-order accurate discretization of the viscous terms. At the immersed boundary the third-order accurate immersed boundary scheme was employed.

Details about the computational setup and the flow conditions used for the cylinder calculations are summarized in Table H.4 in Appendix H. At the inflow boundary the velocities are fixed to the free-stream values. The treatment of the remaining primitive variables ( $\rho, p, T$ ) at the inflow typically depends on the local Mach number. For subsonic Mach numbers, the pressure is fixed to the free-stream value and the density is extrapolated using Riemann invariants. The temperature is then obtained from the equation of state. At the outflow, a standard outflow condition was employed, where the velocities are extrapolated from the fluid domain to the guard cells. For the top and bottom boundary condition, the primitive variables are extrapolated into the guard cells using a second-order accurate extrapolation scheme. The viscosity for these simulations is set to a constant value depending on the Reynolds number. For all calculations, the flow field was initialized with the potential flow solution provided in Eq. (G.1).

Sufficient grid resolution around the cylinder is crucial to obtain accurate results for the lift and drag coefficients. In addition, the wake region has to be resolved accurately to capture the von Kármán vortex shedding. A schematic of the grid employed for the cylinder around the immersed geometry is displayed in Fig. 9(a). Note that the grid schematic in Fig. 9(a) only shows the boundaries of the blocks used in the block structured computational domain. The blocks contain 20 grid points in each of the coordinate directions. The wake region was resolved with a grid spacing of  $D/\Delta x \approx 60$  for a region approximately seven cylinder diameters downstream of the center of the cylinder. This grid resolution is comparable to the grid spacing reported by Mittal et al. [13]. At this grid resolution the lift and drag coefficients are sufficiently grid converged. The computational domain is  $80D$  wide and  $80D$  tall to avoid domain confinement effects and wave reflections from the domain boundaries, which could lead to a significant error when computing the lift and the drag force around the cylinder. These observations are similar to what has been reported for incompressible simulations by Brehm and Fasel [17]. A detailed discussion regarding the dependence of the computed flow field on the location of the upper and lower domain boundaries for the incompressible flow past a circular cylinder was presented by Behr [35].

The steady simulation results were quantified by extracting the length of the separation bubble, the location of the counter rotating vortices in the cylinder wake, and the flow separation point on the cylinder surface (see Fig. 9(b)). Fig. 10 shows streamlines and iso-contours of spanwise vorticity,  $\omega_z$ , for the steady flow cases. The steady separation region grows in length as the Reynolds number increases. A comparison of the accumulated data obtained in the current simulation and data published in the literature is provided in Table 1. All numerical values are in excellent agreement with the previously published data.

Snapshots of the flow fields around the cylinder at larger Reynolds numbers ( $Re = 100$  and  $Re = 200$ ) are shown in Fig. 11. The strong shear layer instability in these cases causes the vortex shedding to set in rapidly. For both investigated cases, the contours of the spanwise vorticity do not reduce significantly in amplitude in the wake of the cylinder, which



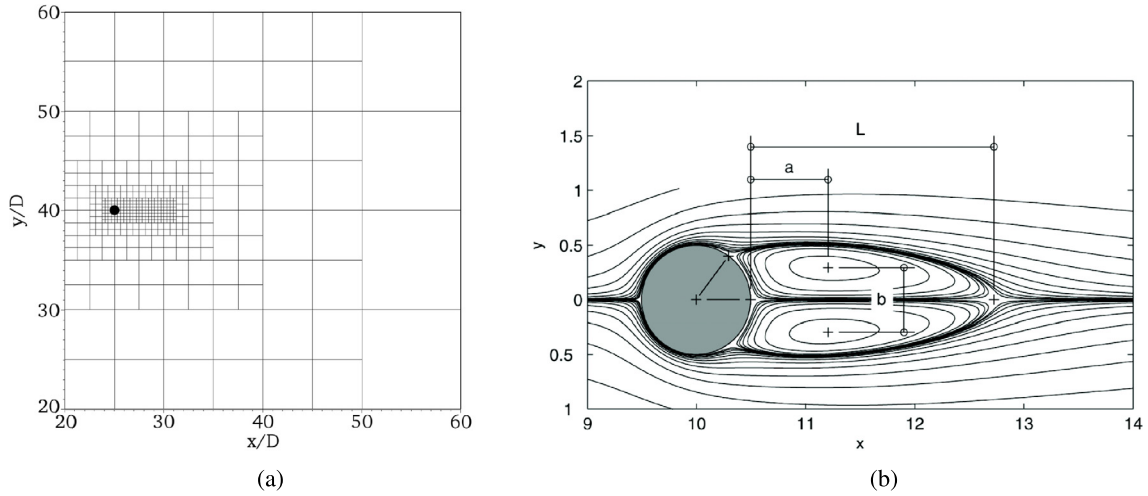


**Fig. 9.** (a) Grid topology and immersed geometry employed for cylinder simulations block structured Cartesian mesh. (b) Nomenclature used to quantitatively describe the steady cylinder flow (adjusted from Linnick [6]).

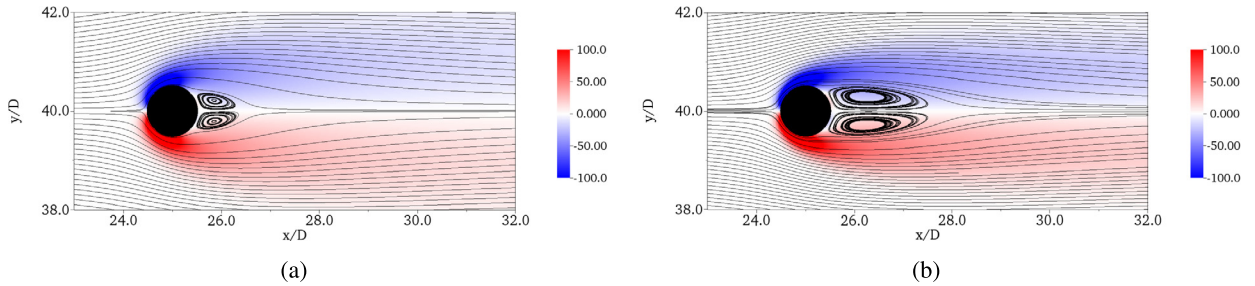


**Fig. 10.** Iso-contours of spanwise vorticity and streamlines for steady cylinder flow of (a)  $Re = 20$  and (b)  $Re = 40$ .

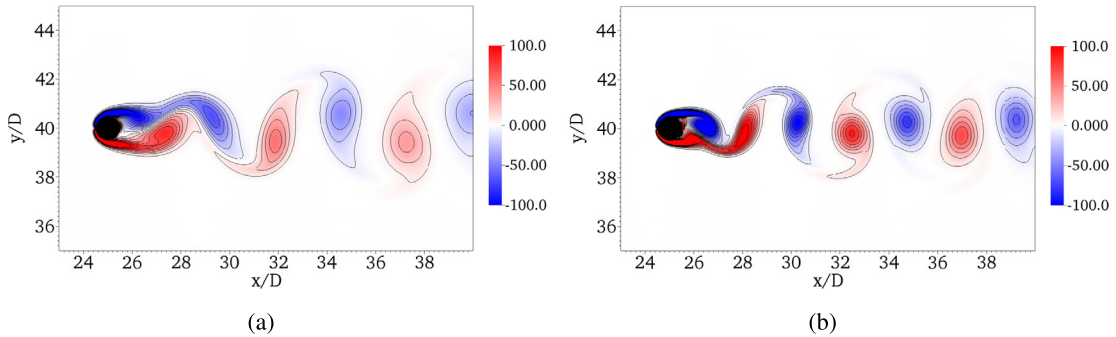


**Fig. 11.** Contours of constant spanwise vorticity and streamlines for unsteady cylinder flow of (a)  $Re = 100$  and (b)  $Re = 200$ .

indicates that the wake is sufficiently resolved for the given flow conditions. Furthermore, no numerical artifacts are observed at the coarse-fine grid interfaces employing fourth-order accurate guard cell filling. These observations suggest that the quality of the block structured grid and numerical methods employed for the cylinder simulations are adequate for the current analysis. Since the flow becomes unsteady, a different set of numerical parameters describing the temporal evolution of the lift coefficient,  $c_L$ , drag coefficient,  $c_D$ , and non-dimensional frequency, the Strouhal-number defined as  $St = fD/U_\infty$ , are used. Due to the unsteadiness of the flow, it is important to compare the average values of the lift and drag coefficients as well as the amplitude of the sinusoidal variation in time of the lift and drag coefficient. The results for the time-averaged lift and drag coefficients, the amplitude of their modulations as well as the Strouhal number for the unsteady cylinder cases of the present study are compared to published results in Table 1. All results compare very well with results reported in the literature.

**Table 1**

Comparison of results for steady and unsteady cylinder flow: Length of separation,  $L$ , location of vortex centers described by  $a$  and  $b$ , angle of separation,  $\Theta$ , Strouhal number,  $St$ , lift coefficient,  $c_L$ , and drag coefficient,  $c_D$ .

	$L$	$a$	$b$	$\Theta$	$c_D$		$L$	$a$	$b$	$\Theta$	$c_D$
$Re_D = 20$ :						$Re_D = 40$ :					
Fornberg [36]	0.91	—	—	45.7°	2.00		2.24	—	—	55.6°	1.50
Dennis [37]	0.94	—	—	43.7°	2.05		2.35	—	—	53.8°	1.52
Coutanceau [38]*	0.93	0.33	0.46	45.0°	—		2.13	0.76	0.59	55.8°	—
Tritton [34]*	—	—	—	—	2.09		—	—	—	—	1.59
Mittal [13]	—	—	—	—	—		—	—	—	—	1.53
Henderson [39]	—	—	—	—	—		—	—	—	—	1.54
Marella [40]	—	—	—	—	—		—	—	—	—	1.52
Linnick [6]	0.93	0.36	0.43	43.5°	2.06		2.28	0.72	0.60	53.6°	1.54
Brehm [17]	0.94	0.36	0.43	43.5°	2.08		2.29	0.72	0.60	52.4°	1.57
<b>present study</b>	<b>0.96</b>	<b>0.36</b>	<b>0.42</b>	<b>44°</b>	<b>2.02</b>		<b>2.26</b>	<b>0.72</b>	<b>0.58</b>	<b>52.9°</b>	<b>1.51</b>

(\*) Results from Coutanceau [38] are extrapolated to  $\lambda = 0$ .

	$St$	$c_D$	$c_L$		$St$	$c_D$	$c_L$
$Re_D = 100$ :				$Re_D = 200$ :			
Berger [41]*	0.16–0.17	—	—		0.18–0.19	—	—
Liu [42]	0.165	$1.35 \pm 0.012$	$\pm 0.339$		0.192	$1.31 \pm 0.049$	$\pm 0.69$
Linnick [6] ( $\lambda = 0.056$ ) <sup>⊙</sup>	0.169	$1.38 \pm 0.010$ <sup>~</sup>	$\pm 0.337$		0.199	$1.37 \pm 0.046$ <sup>~</sup>	$\pm 0.70$
Linnick [6] ( $\lambda = 0.023$ ) <sup>⊙</sup>	0.166	$1.34 \pm 0.009$	$\pm 0.333$		0.197	$1.34 \pm 0.044$	$\pm 0.69$
Mittal [13]	—	1.35	—		—	—	—
Henderson [39]	—	1.35	—		—	—	—
Marella [40]	—	1.36	—		—	—	—
Belov [43]	—	—	—		0.193	$1.19 \pm 0.042$	$\pm 0.64$
Rogers, Kwak*	—	—	—		0.185	$1.23 \pm 0.050$	$\pm 0.65$
Miyake et al.*	—	—	—		0.196	$1.34 \pm 0.043$	$\pm 0.67$
Brehm [17]	0.170	$1.38 \pm 0.011$ <sup>~</sup>	$\pm 0.342$		0.198	$1.38 \pm 0.044$ <sup>~</sup>	$\pm 0.70$
<b>present study</b>	<b>0.165</b>	<b><math>1.32 \pm 0.01</math></b>	<b><math>\pm 0.32</math></b>		<b>0.192</b>	<b><math>1.3 \pm 0.04</math></b>	<b><math>\pm 0.66</math></b>

Note: (\*) In Belov, (⊙) Linnick and Fasel used two different domain sizes; parameter  $\lambda$  is the ratio of cylinder diameter,  $D$ , to domain height. (\*) Experimental results. (~) Approximate values.

**Table 2**

Comparison of results for the steady ( $Re_D = 100$ ) and unsteady ( $Re_D = 350$ ) flows around a sphere considering the center of the recirculation region ( $x_c/D$ ,  $y_c/D$ ), the length of recirculation region ( $L_b/D$ ), and the Strouhal number ( $St$ ).

	$x_c/D$	$y_c/D$	$L_b/D$		$St$
$Re_D = 100$ :				$Re_D = 350$ :	
Mittal [13]	0.742	0.278	0.84	Mittal [13]	0.135
Johnson and Patel [44]	0.75	0.29	0.88	Johnson and Patel [44]	0.137
Taneda [45]	0.745	0.28	0.8	Taneda [45]	—
Marella [40]	—	—	0.88	Marella [40]	0.133
<b>present study</b>	<b>0.78</b>	<b>0.3</b>	<b>0.9</b>	<b>present study</b>	<b>0.132</b>

## 5.2. Flow around a sphere

To validate the immersed boundary method for a 3D problem the flow around a sphere is simulated. The flow around the sphere is computed for two Reynolds numbers,  $Re_D = 100$  and  $Re_D = 350$ , which lead to steady and unsteady solutions, respectively. The results are compared to data from previous numerical and experimental studies. The domain setup and flow conditions used for the sphere simulations are summarized in Table H.4 in Appendix H. The free-stream conditions are similar to the flow conditions used for the cylinder simulations. Compared to the 2D simulations, the computational domain size for the sphere flow simulations can be slightly reduced based on results reported by Mittal et al. [13]. The grid employed for the sphere simulations is similar to the one used for the cylinder simulations with approximately sixty grid points per sphere diameter in the wake. The wake grid is extended approximately seven diameters downstream. Away from the sphere the grid spacings increases quickly in order to reduce the number of grid points and the computational cost of the simulations. The boundary conditions at the six domain boundaries are identical to the ones described for the cylinder flow simulations.

The results for the sphere simulation with  $Re_D = 100$  are displayed in Fig. 12. The spanwise vorticity contours and streamlines around the sphere are plotted in the  $z = 0$  symmetry plane. The pressure distribution on the surface of the sphere is smooth. No oscillations can be observed which suggests that the immersed boundary scheme does not induce spurious oscillations for the pressure field in the vicinity of the immersed boundary. A quantitative comparison between the results obtained in the present study and results published in the literature for the steady cases is given in Table 2. The results compare well with the results reported in the literature.

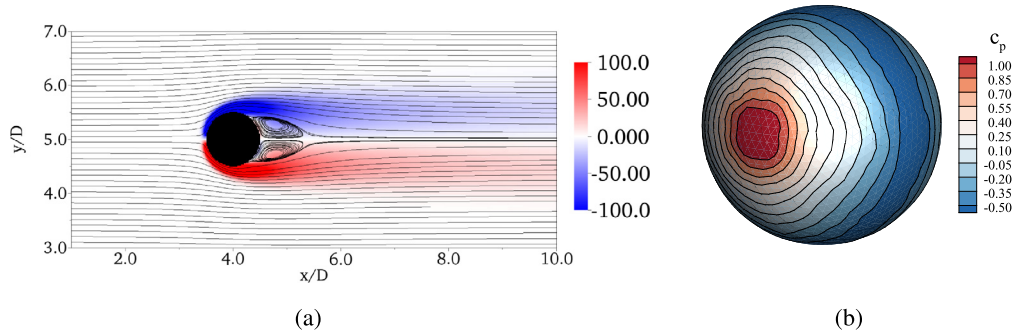


**Fig. 12.** (a) Contours of streamwise vorticity and streamlines of the flow around a sphere. (b) Pressure coefficient distribution on the surface of the sphere.

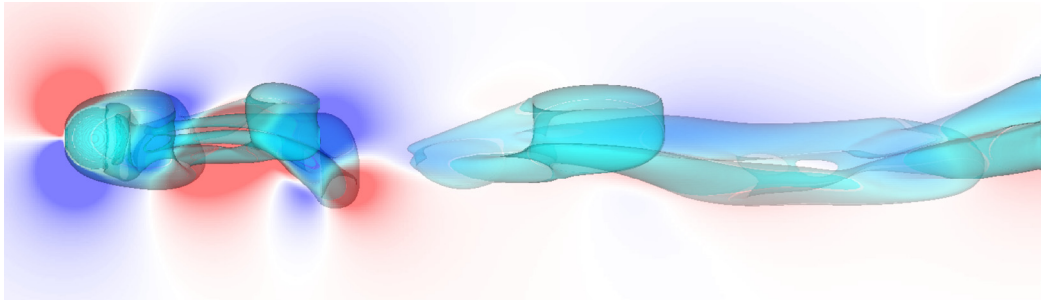


**Fig. 13.** Iso-contours of  $v$ -velocity in the  $z = 0$  symmetry plane (ranging from  $-3$  to  $3$ ) and a  $Q$ -criterion iso-surface with  $Q = 1$ .

For the unsteady case ( $Re_D = 350$ ), iso-contours of  $v$ -velocity in the  $z = 0$  symmetry plane (ranging from  $-3$  to  $3$ ) and a  $Q$ -criterion iso-surface with  $Q = 1$  are displayed in Fig. 13. The contours clearly indicate that the flow field is unsteady and as observed in the literature, vortex loops appear in the wake. The Strouhal number obtained after long time-integration compares well with the results published in the literature (Table 2). The results of these validation cases confirm that the current immersed boundary method is well suited to compute low Reynolds number flows around 2D and 3D geometries. It was shown that the immersed boundary method leads to accurate results while being computationally efficient.

## 6. Applications

In this section, results are presented where the immersed boundary method is applied to various flow problems that are relevant for ongoing laminar to turbulent transition research. To demonstrate that this method can be used for high speed Direct Numerical Simulations (DNS), the propagation of a Tollmien Schlichting wave in a high speed boundary layer was simulated. Additionally, this method was employed to physically resolve a porous wall and to investigate the influence of the porous wall on the transition process of a hypersonic boundary layer. The effect of the porous wall on the laminar-turbulent transition process in the linear and nonlinear stability regime is briefly discussed. Furthermore, the flow past a roughness element in a subsonic boundary layer is simulated in 2D and 3D.

### 6.1. Flat plate

The present immersed boundary approach was used to compute the propagation of a second mode disturbance wave in an  $M = 6$  boundary layer flow. The flow conditions which were chosen according to Sandham et al. [46] are summarized in Table H.5 in Appendix H. A two-dimensional disturbance wave was introduced by a volume forcing term with a spatial wave length (based on the displacement thickness) of  $\lambda_x/\delta^* = 3$ . Isothermal wall boundary conditions were applied for these calculations. The temporal direct numerical simulation results based on the current third-order accurate immersed boundary method are compared to results with a formally second-order accurate immersed scheme discussed in Hader and Fasel [47], which is referred to as IBT, and results for a body-fitted grid similar to Laible and Fasel [22], which is referred to as “body-fitted” and serves as the reference solution. At regular grid points, the ninth-order accurate and eighth-order accurate discretizations were used for the convective and viscous terms, respectively.

The wall-normal amplitude distributions of the  $u$ -velocity, and disturbance pressure are displayed in Fig. 14. For the results shown here, a grid spacing at the wall of  $\Delta y = 1 \cdot 10^{-3}$  was used for the current immersed boundary method and a wall grid spacing of  $\Delta y = 5 \cdot 10^{-4}$  was employed for the IBT. Although the resolution at the wall was finer for the IBT scheme, the results were found to be less accurate compared to those obtained with the new method. In addition, the wall-normal pressure disturbance distribution at the wall deviates slightly from the reference solution for the IBT scheme.

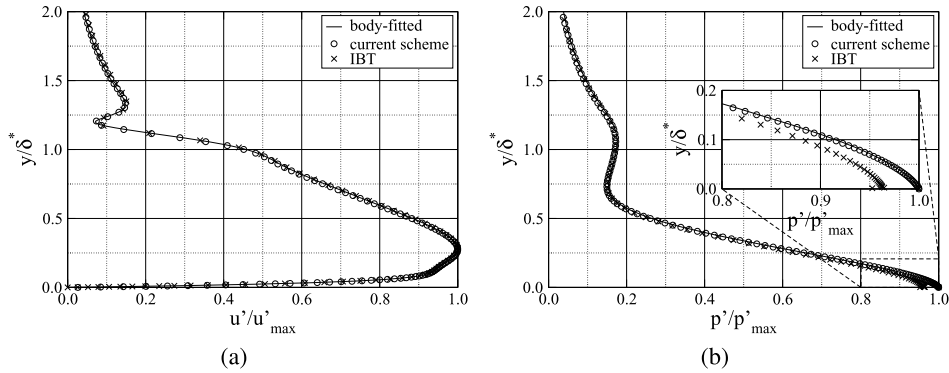


**Fig. 14.** Wall-normal amplitude distributions of (a)  $u$  disturbance velocity, and (b) disturbance pressure. Only every second grid point in wall normal direction is displayed.

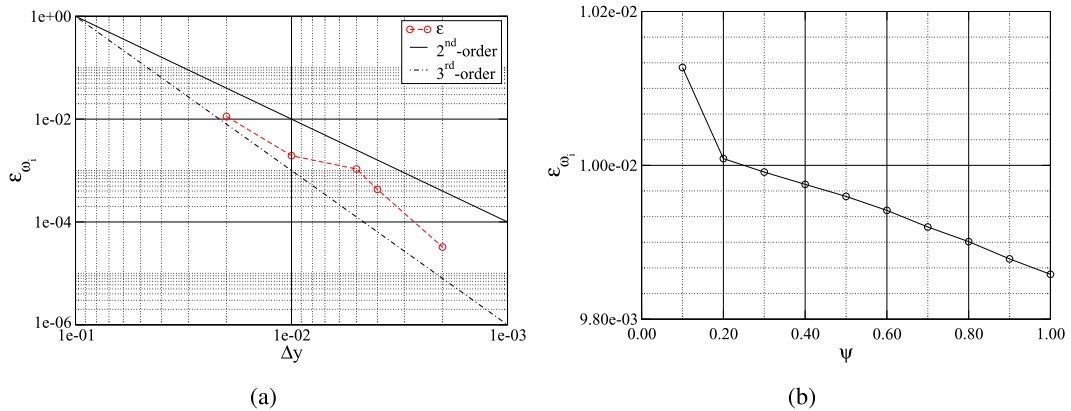


**Fig. 15.** (b) Error in temporal growth rate,  $\omega_i$ , for different boundary distances,  $0 < \psi < 1$ . (a) Order-of-accuracy study with respect to the error in the temporal growth rate  $\varepsilon_{\omega_i}$ .

With the presented immersed boundary scheme the wall normal amplitude distributions are in excellent agreement with the reference solution.

To further investigate the accuracy of the immersed boundary method, the growth rate of the instability wave was determined for different grids. For the order-of-accuracy study of the numerical scheme, the grid was chosen to be equidistant until  $y/\delta^* = 2$  to avoid effects on the error convergence due to grid stretching. Fig. 15(a) displays the error in the temporal growth rates,  $\omega_i$ , for different grid spacing in the equidistant region. The solution based on the finest grid was used as the reference solution for the coarser grids to determine the order of the scheme. The order-of-accuracy study confirms that the immersed boundary scheme is third-order accurate with respect to the error in the temporal growth rate. To demonstrate the dependence of the numerical solution on the boundary distance,  $\psi$ , Fig. 15(b) displays the relative error of the temporal growth rate,  $\varepsilon_{\omega_i}$ , for different boundary distances. Almost no change of the growth rate with respect to the boundary distance can be detected. The relative error is approximately 1% for all investigated boundary distances.

## 6.2. Porous wall

Next, the immersed boundary method was employed for Temporal Direct Numerical Simulations (TDNS) of instability waves in a Mach 6 boundary layer with porous walls. The same flow conditions as for the flat plate simulations are employed for this study (see Table H.5 in Appendix H). The main parameters of the porous wall are the depth of the porous layer,  $d$ , the porosity,  $\phi$ , and the number of pores per wave length,  $n_p$ , as shown in the schematic in Fig. 16. The porosity is defined as the ratio of the porous surface to the total surface ( $\phi = b/s$ ). A parameter study by Hader et al. [47] revealed the geometric dimensions for which the porous coating most effectively attenuates the growth of disturbances in the boundary layers. For the optimal parameter combination, significant stabilization of the temporal/spatial growth of the instability waves is observed in experiments and computations (see for example Malmuth et al. [48], Fedorov et al. [49,50], Brès [51], and Sandham [46]).

To model the effects of porous walls in the context of Linear Stability Theory (LST), Fedorov et al. [49] derived suitable boundary conditions at the wall. From this LST analysis it was found that the so-called Ultrasonically Absorptive Coating (UAC) is stabilizing the flow over a wide range of frequencies and Reynolds numbers. A comparison between DNS with a

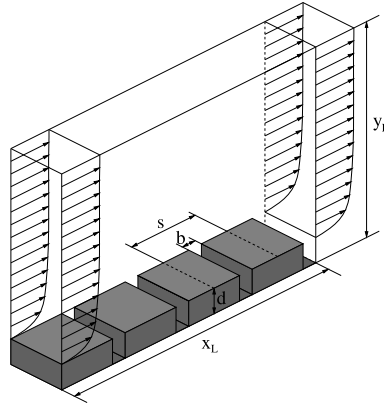
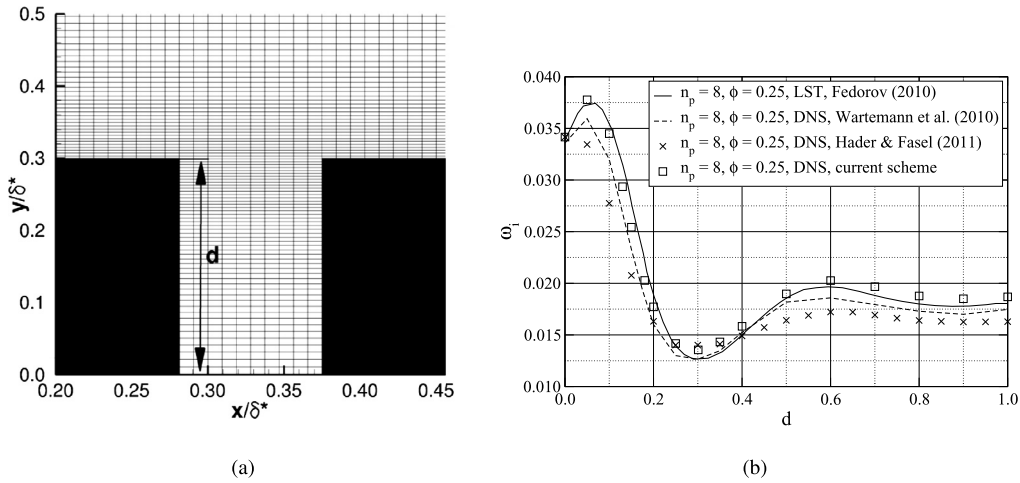


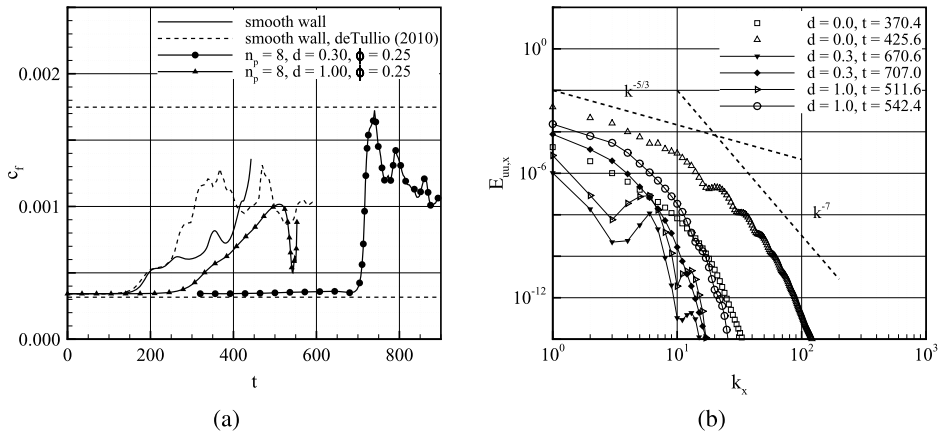
Fig. 16. Schematic of porous wall.

Fig. 17. (a) Grid used for porous wall simulations. (b) Temporal growth rate,  $\omega_i$ , obtained for varying cavity depths.

body-fitted grid and LST using porous wall boundary conditions was provided by Fedorov [52]. Results from both methods, DNS and LST, were in good agreement for the investigated parameter space. Wartemann et al. [53] carried out another comparison of LST and DNS utilizing a body-fitted grid. This investigation covered a larger parameter space than the investigation by Fedorov [52]. The LST and DNS results presented in Wartemann et al. [53] were in overall good agreement. For the porous wall simulations presented here, grid points were clustered around the top of the cavities as displayed in Fig. 17(a). A comparison between theoretical investigations by Fedorov [49], the DNS results of Wartemann [53] and the DNS employing an IBT as discussed in Hader and Fasel [47] and the immersed boundary method discussed in this paper is given in Fig. 17(b). The current simulation results are in excellent agreement with the theoretical results by Fedorov [52]. The current immersed boundary method predicts the influence of the porous wall on the linear stability of the high speed boundary layer much better than the IBT approach previously employed by Hader et al. [47]. The region of destabilization for very shallow cavities ( $0 \leq d \leq 0.1$ ), which could not be detected with the IBT approach, can be captured with the present method.

Since the nonlinear stability regime is of more practical interest, the present immersed boundary method was also employed to investigate the influence of the porous wall on the nonlinear stability mechanisms. Compared to the linear stability regime, the nonlinear regime is characterized by large, high frequency disturbance amplitudes and strong interaction between the baseflow and the various disturbance modes. The laminar to turbulent breakdown for high speed flows is traditionally initialized with so-called controlled transition scenarios (for more details see Hader et al. [54,55]). Utilizing the immersed boundary method for these types of flows poses a rigorous test on the capabilities of the current scheme. The immersed boundary method was successfully employed to simulate well into the transition region. The investigation revealed that the porous walls are not only stabilizing in the linear but also in the nonlinear regime. A common measure to check if transition onset occurred is to compute the averaged skin friction coefficient which in non-dimensional quantities is defined as

$$c_f = \frac{2}{Re} \mu_w \frac{\partial u}{\partial y}, \quad (36)$$



**Fig. 18.** (a) Comparison of skin friction evolution for smooth wall and porous wall cases for different breakdown scenarios. (b) Power spectrum of streamwise disturbance velocity for different cavity depths,  $d$ .

where,  $\mu_w$  is the viscosity at the wall obtained with Sutherland's law. A comparison of the temporal evolution of the averaged skin friction for the smooth and porous wall cases and for the so-called fundamental breakdown scenario is displayed in Fig. 18(a). As a reference, the laminar and turbulent estimates of the skin friction for the given flow conditions are plotted. The results show that the skin friction deviates from the laminar value at a much later time when porous walls are present. In Fig. 18(b) the power spectrum of streamwise disturbance velocity for different cavity depths is shown. The energy spectra indicate that the smooth wall case progresses much faster into turbulence compared to the porous wall cases. The results demonstrate that the pores can effectively delay transition onset in high speed flows. In addition, the cavity depth that was found to attenuate the growth of the primary stability wave also most effectively delays the transition onset to a later time compared to the less effective pore geometry.

This application of the immersed boundary method shows that the present immersed boundary method is a useful tool for transition research. The computational grid is generated automatically regardless of geometric complexity. No additional time step restrictions or robustness issues, when compared to body fitted approaches, were encountered when applying the immersed boundary method to this transition research problem.

### 6.3. Discrete roughness

In the last test case, the immersed boundary method is used to simulate the effect of a discrete roughness element on a subsonic boundary layer flow over a flat plate. For these simulations the grid is refined around the roughness element to sufficiently resolve the immersed geometry as well as the boundary layer. A schematic of the grid around the circular roughness element is provided in Figs. 19(a) and 19(b). The grid topology is displayed by visualizing the block boundaries. Each block contains 18 grid points in each coordinate direction. For these low Reynolds number conditions we were able to obtain a wall spacing of  $y^+ \approx 1$  (calculated by assuming turbulent flow estimates). The roughness element is located 60 displacement thicknesses downstream of the flat plate leading edge. The discrete roughness element has the shape of a half circle in 2D and a half sphere in 3D. The roughness height was chosen to match the boundary layer thickness at the inflow of the computational domain. The inflow at  $x = 0$  in Fig. 19(a) is located 15 boundary layer displacement thicknesses downstream of the flat plate leading edge. The roughness element height is relatively large and, thus, poses a rigorous test problem for the immersed boundary method. For this roughness height, no inflow disturbances have to be imposed on the boundary layer flow to trigger unsteadiness in the shear layer created by the presence of the roughness element. For these simulations, the flow is initialized with a boundary layer similarity solution obtained with a compressible similarity solver for  $M = 0.1$ . The Reynolds number based on the inflow displacement thickness is  $Re_{\delta^*} = 164.75$ . The flow conditions and the computational setup for these simulations are summarized in Table H.6 (Appendix H). A snapshot of vorticity contours for the  $M = 0.1$  case is provided in Fig. 20. A strong upstream effect of the roughness element is observed for this low Mach number condition. The contours of spanwise vorticity show that vortex shedding sets in for these flow conditions. No numerical artifacts due to the immersed boundary treatment were observed in the flow field.

The 3D simulations were conducted considering the same flow conditions and grid layout in the  $z = 0$  symmetry plane as for the 2D simulation. A top view of the mesh is provided in Fig. 19(b). In spanwise direction, the mesh starts coarsening out 30 displacement thicknesses away from the roughness element. Iso-contours of the  $v$ -velocity in the  $z = 0$  symmetry plane and a  $Q$ -criterion iso-surface ( $Q = 0.01$ ) are shown in Fig. 21. A steady horse shoe vortex is wrapping around the front of the half-spherical roughness element. In the wake of the roughness element unsteady vortices are generated and subsequently break down to smaller flow structures. This test case was chosen to demonstrate the robustness of the immersed boundary method. As for the steady test case, no numerical artifacts were observed in the flow fields or in the pressure distribution on the immersed geometry.



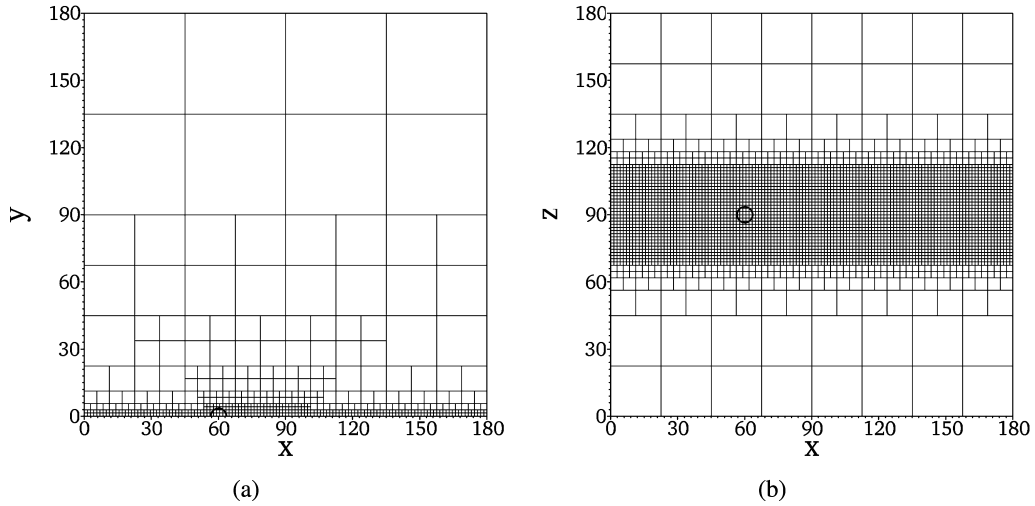


**Fig. 19.** Grid topology employed for 2D and 3D discrete roughness simulations: (a) Side view and (b) top view. Only block boundaries are shown.

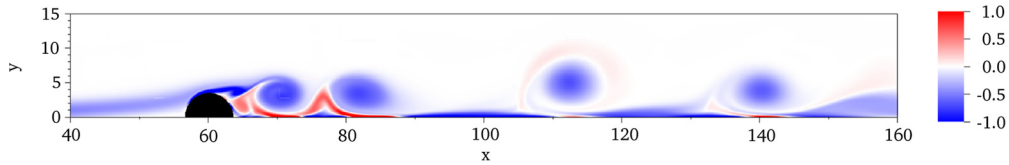


**Fig. 20.** Instantaneous snapshots of spanwise vorticity contours for the  $M = 0.1$  flow extracted at (a)  $t = 160$ .

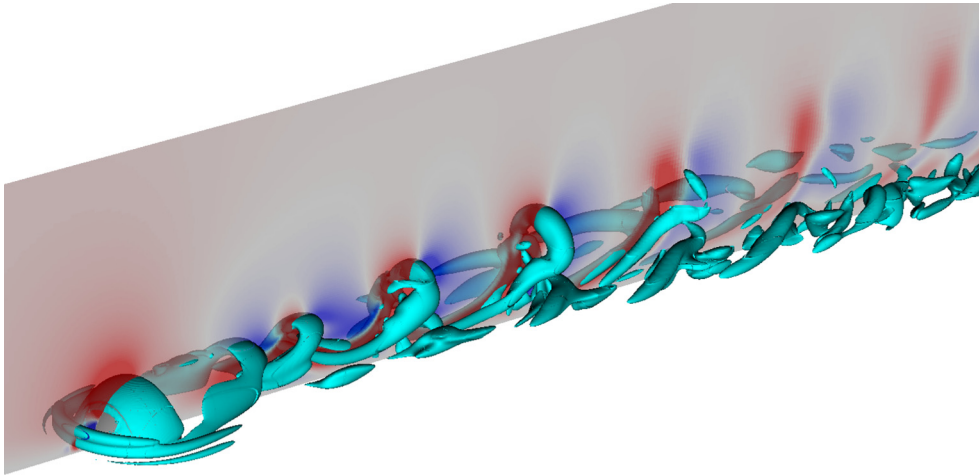


**Fig. 21.** Iso-contours of  $v$ -velocity in  $z = 0$  symmetry plane and contours of constant  $Q = 0.01$ .

## 7. Conclusion

A novel higher-order accurate immersed boundary method for solving the compressible Navier–Stokes equations was presented. The key feature of this method is that the irregular FD stencils in the vicinity of the immersed boundary are optimized with respect to numerical stability. This is a very unique feature because commonly only the order-of-accuracy is taken into consideration when discretizing the governing equations in the vicinity of the immersed boundary. In the optimization procedure, the non-linear compressible Navier–Stokes equations are linearized and, thus, the optimization procedure for the irregular FD stencils is solely based on linear stability. A multi-dimensional optimization procedure is avoided by isolating the irregular FD stencil from the rest of the computational domain. This simplification, implies that

the sufficient condition for numerical stability of the update matrix cannot be strictly guaranteed. However, no numerical stability issues have been encountered for any of the test cases or applications this method has been applied to. The accrued computational cost for computing the irregular stencil coefficients is negligible in comparison to the cost of the overall numerical scheme.

The immersed boundary method was derived to allow for arbitrary order-of-accuracy. Employing the method of manufactured solutions, the formal order-of-accuracy of the second-order and third-order versions in  $L_\infty$ -norm (third and fourth-order accuracy in  $L_2$ -norm) of the immersed boundary method was verified for the convective and viscous terms on uniform and stretched meshes in 2D and 3D. The 1D and 2D linear matrix stability analysis results confirm that the immersed boundary method is linearly stable. A comparison with three other immersed boundary methods, which can be obtained by choosing particular values for the free stencil coefficient, demonstrates the improved stability characteristics of the present scheme.

The flows around a cylinder and a sphere serve as canonical test problems to validate the current immersed boundary method. No numerical artifacts can be observed in the flow field, such as spurious numerical oscillations in the pressure distribution around the immersed boundary, which has been frequently observed for other immersed boundary methods. The computational results for the 2D and 3D validation cases are in excellent agreement with numerical and experimental results reported in the literature. In addition, the current immersed boundary method has been successfully applied to multiple fluid dynamics problems relevant for ongoing transition research. The simulation results for the hypersonic flow over a porous wall demonstrated that the numerical accuracy in the vicinity of the porous wall is crucial to accurately capture the stability characteristics of the baseflow. It is well-known that employing higher-order accurate numerical schemes (p-refinement) is computationally more efficient than locally reducing the grid spacing (h-refinement). For all investigated cases, the new immersed boundary method has been proven to lead to accurate results while being robust, stable and computationally efficient.

## Acknowledgements

The authors gratefully acknowledge the contributions from the LAVA group at Applied Modeling Simulation Branch NASA Ames Research Center (ARC). The work was partially funded by the Applied Modeling Simulation Branch at NASA ARC and the Hypersonic Center for Laminar Turbulent Transition Research.

## Appendix A. Interior discretization for convective terms

The stencil coefficients for the interior scheme are derived by utilizing the Taylor series expansion of  $\phi_k$  in Eq. (3) and balancing the terms on the left and right-hand-sides to the desired order of accuracy. This leads to a system of equations in the form

$$\underline{M}\mathbf{c} = \mathbf{r}, \quad (\text{A.1})$$

with

$$\underline{M} = \begin{bmatrix} \dots & 1 & 1 & 1 & \dots \\ \dots & \Delta x_{i-1} & 0 & \Delta x_{i+1} & \dots \\ \dots & \frac{(\Delta x_{i-1})^2}{2!} & 0 & \frac{(\Delta x_{i+1})^2}{2!} & \dots \\ \dots & \vdots & \vdots & \vdots & \dots \end{bmatrix}, \quad \mathbf{c} = \begin{bmatrix} \vdots \\ c_{i-1} \\ c_i \\ c_{i+1} \\ \vdots \end{bmatrix}, \quad \text{and} \quad \mathbf{r} = \begin{bmatrix} 0 \\ 1 \\ \vdots \\ \alpha \frac{\Delta x^n}{(n+1)!} \end{bmatrix},$$

where  $\Delta x_{i\pm 1} = x_{i\pm 1} - x_i$  and  $n$  is the order of accuracy of the FD scheme. In accordance to the chosen discretization in Laible and Fasel [22], the  $n$ th-order accurate upwind stencils are calculated with  $n \in \{9, 7, 5, 3, 1\}$  and  $\alpha \in \{-1500, 72, -12, 0.6, -1\}$ . For the ninth-order accurate upwind-biased FD scheme with  $\alpha = -1500$  and equidistant grid spacings, solving the linear system of Eq. (A.1) leads to the FD coefficient vector in the form

$$\mathbf{c} = \frac{1}{\Delta x} \left[ \frac{-73}{60480}, \frac{85}{6048}, \frac{-5}{64}, \frac{145}{504}, \frac{-265}{288}, \frac{5}{48}, \frac{215}{288}, \frac{-95}{504}, \frac{55}{1344}, \frac{5}{864}, \frac{23}{60480} \right].$$

Additional details about the higher-order upwind-biased FD scheme using centered grid stencils can be found in Zhong [23].

## Appendix B. IIM stencil optimization procedure

To demonstrate the optimization procedure, the 1D Euler equations were discretized on a computational domain extending from  $x \approx 0.35$  to  $x \approx 0.62$  with a total of  $N = 31$  grid points (see Fig. B.22(a)). For the analysis of the numerical scheme, it was assumed that the solution is prescribed at the right boundary for all grid points, which are needed to compute the node-centered upwind FD stencils. This procedure isolates the effect of the immersed boundary on the stability of the numerical scheme. To illustrate the optimization procedure and study the stability properties of the numerical scheme we chose flow conditions that are realistic and relevant for ongoing hypersonic transition research. The flow conditions

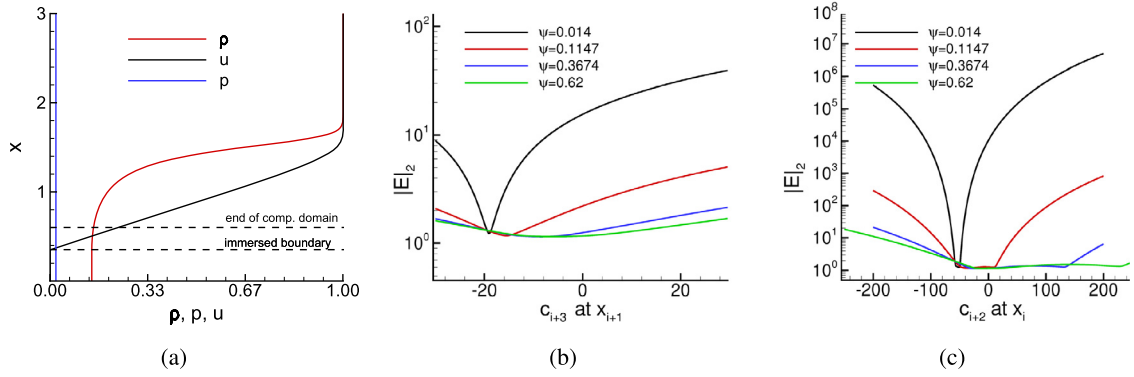


**Fig. B.22.** a) Velocity, density, and pressure profiles used for the analysis of the 1D Euler system. Examples of  $|E|_2$  curves as a function of the free parameter; b)  $c_{i+3}|_{x_{i+1}}$  and c)  $c_{i+2}|_{x_i}$  of the two optimization problems for different boundary distances,  $\psi$ .

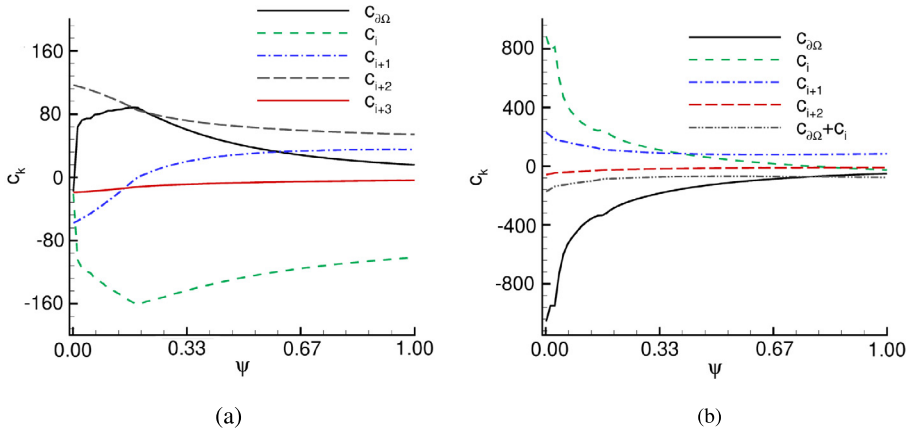


**Fig. B.23.** Dependence of the irregular FD stencil coefficients at (a)  $x_{i+1}$  and (b)  $x_i$  on the boundary distance,  $\psi$ .

were chosen in accordance with numerical investigations of the transition process of a Mach 6 boundary layer flow passing over a porous wall presented in Section 6.2. The velocity, pressure, density, and temperature profiles were obtained with a similarity solver for compressible boundary layers. Fig. B.22(a) shows the velocity, pressure, and density profiles which are used in this study. All quantities are normalized with their respective free-stream values. The different profiles are calculated for a Mach number of  $M = 6$ , a free-stream temperature of  $T_\infty = 216.65$  K, a heat capacity ratio of  $\gamma = 1.4$ , and a Prandtl number of  $Pr = 0.72$ . The wall boundary condition for the temperature is adiabatic, and the viscosity is calculated using Sutherland's law. This setup leads to a ratio of adiabatic wall temperature,  $T_{aw}$ , to free-stream temperature,  $T_\infty$ , of  $T_{aw}/T_\infty \approx 7.03$ . The boundary layer flow was turned into a 1D problem by using the streamwise velocity distribution as a 1D velocity field. In the vicinity of the immersed boundary, the velocity profile is nearly linear. This simplified test case serves the purpose of presenting the procedure on how to obtain stencil coefficients in the vicinity of the wall by applying an optimization procedure.

Figs. B.22(b) and B.22(c) show the dependence of the  $L_2$ -norm of the perturbation matrix  $\mathbf{E}$  on the free parameters,  $c_{i+3}|_{x_{i+1}}$  and  $c_{i+2}|_{x_i}$ . In the optimization procedure, we seek the solutions for  $c_{i+3}|_{x_{i+1}}$  and  $c_{i+2}|_{x_i}$  that minimize the  $L_2$ -norm of  $\mathbf{E}$ . The two free parameters  $c_{i+3}|_{x_{i+1}}$  and  $c_{i+2}|_{x_i}$  are determined by solving two 1D optimization problems sequentially. In the first optimization problem, the stencil coefficient  $c_{i+3}|_{x_{i+1}}$  associated with the irregular FD stencil at  $x_{i+1}$  applied at grid point  $x_{i+3}$ , is taken as the first free parameter, and in the second optimization problem, the stencil coefficient  $c_{i+2}|_{x_i}$ , associated with the irregular FD stencil at  $x_i$  applied at grid point  $x_{i+2}$ , is used as the second free parameter. The grid points where the stencil coefficients  $c_{i+3}|_{x_{i+1}}$  and  $c_{i+2}|_{x_i}$  are applied to are farthest away from  $x_{i+1}$  and  $x_i$ , respectively. Consequently, their absolute values are considerably smaller compared to the other stencil coefficients. Figs. B.22(b) and B.22(c) show a very smooth behavior of the  $L_2$ -norm of  $\mathbf{E}$  as a function of  $c_{i+3}|_{x_{i+1}}$  and  $c_{i+2}|_{x_i}$ , thus allowing for fast convergence of extremum seeking algorithms. As the boundary distance  $\psi$  increases, the relatively flat region near the minimum value of the function becomes larger, which consequently decreases the sensitivity of the objective function to small deviations from the optimal values of  $c_{i+3}|_{x_{i+1}}$  or  $c_{i+2}|_{x_i}$ . Figs. B.23(a) and B.23(b) show how the stencil coefficients at the two irregular grid points  $x_i$  and  $x_{i+1}$  adjust to different values of the normalized boundary distance,  $\psi$ . The value of the

last coefficients,  $c_{i+3}|_{x_{i+1}}$  and  $c_{i+2}|_{x_i}$ , in the irregular FD stencils is the smallest value compared to the other coefficients in the stencil. For large boundary distances,  $\psi$ , the values of the optimal stencil coefficients change very little. As  $\psi$  approaches zero, the optimal FD stencil coefficients at  $x_{i+1}$  and at  $x_i$  behave significantly different. The coefficients of the irregular FD stencil at  $x_{i+1}$  are well behaved for small  $\psi$  (approaching zero). For  $\psi = 0^+$ , the stencil coefficient  $c_{\partial\Omega}|_{x_{i+1}}$  converges towards the value of  $c_i|_{x_{i+1}}$ . The coefficients,  $c_{\partial\Omega}|_{x_i}$  and  $c_i|_{x_i}$ , which belong to the irregular FD stencil at  $x_i$  become very large as the boundary distance  $\psi$  approaches zero. However, the sum of these two coefficients  $c_{\partial\Omega}|_{x_i} + c_i|_{x_i}$  behaves well as the boundary distance becomes very small. In the limit  $\psi = 0^+$ , the two grid points  $x_i$  and  $x_{\partial\Omega}$  are identical and the two FD stencil coefficients  $c_{\partial\Omega}|_{x_i}$  and  $c_i|_{x_i}$  are applied at the same grid point. Note that the increase in  $|c_{\partial\Omega}|_{x_i} + c_i|_{x_i}|$  for  $\psi$  approaching zero is moderate and does not constitute a singularity at  $\psi = 0$ . In order for the numerical scheme to be well-conditioned it is essential that there is no singularity present for  $\psi$  approaching zero.

The computational cost for obtaining the optimal stencil coefficients is small in comparison to the overall cost of the numerical scheme considering that for a 3D simulation with  $N^3$  grid points only  $\mathcal{O}(N^2)$  grid points are irregular. Nevertheless, the optimization routines for the irregular FD stencils were optimized taking advantage of vectorizations and pre-computing analytical expressions. On a Cartesian grid, the irregular FD stencils can be derived analytically (see Eq. (15)) and depend only on a single free parameter that is determined with the above optimization procedure. Furthermore, after the simulation passes the initial transient, where the numerical solution adjusts from the initial condition, the free parameters in the irregular FD stencils generally do not vary significantly. Thus, the optimal coefficients at timestep  $t^n$  serve as an excellent initial guess for the optimization procedure at  $t^{n+1}$ . Furthermore, it was shown in Figs. B.22(b) and B.22(c) that  $|\mathbf{E}|_2$  is well behaved as a function of the free parameter ( $c_{i+3}|_{x_{i+1}}$  or  $c_{i+2}|_{x_i}$ ). This allows for very fast convergence in the optimization procedure. When numerically experimenting with the current method, we noticed that the irregular stencil coefficients can even be frozen from this point forward without compromising the stability of the numerical scheme.

### Appendix C. Summary of immersed boundary method for convective terms

To guide the implementation of the immersed boundary method for the convective terms we provide a summary of the scheme. For the current discussion, we use the same setup as in Fig. 2(b) with an immersed boundary located between grid points  $x_i$  and  $x_{i-1}$ . The immersed boundary method for the convective terms proceeds as follows:

1. Compute stencil coefficients for the calculation of  $\mathbf{F}_x^-$  at irregular grid points applying the WLSQR procedure with all weights set to one except of the grid point closest to the immersed boundary which is set to the non-dimensional boundary distance,  $\psi$ .
2. Compute irregular FD coefficients for the calculation of  $\mathbf{F}_x^+$  for stencils that do not use boundary information. For example, for a third-order accurate FD operator at  $x_{i+2}$  one may use

$$\left. \frac{\partial \phi}{\partial x} \right|_{i+2} = \frac{\phi_i - 6\phi_{i+1} + 3\phi_{i+2} + 2\phi_{i+3}}{6\Delta x} + \mathcal{O}(\Delta x^3).$$

3. Setup system of Eq. (15) for irregular FD stencils that use boundary information and solve for the FD coefficients as a function of the free parameters.
4. Assemble spatial discretization matrix,  $\tilde{\mathbf{A}}$ , (Eq. (16)) and fully coupled discretization matrix,  $\mathbf{A}$ , (Eq. (7)). Each row,  $r$ , of  $\mathbf{D}_x^+$  ( $N_{loc} \times N_{loc}$ ) contains the FD stencil coefficients at grid point  $x_{i+r-1}$ . Based on the analysis of the localization assumption in Brehm and Fasel [20],  $N_{loc}$  is typically equal to the width of the largest irregular FD stencil plus one.
5. Compute matrix  $\mathbf{E}$  (Eq. (8)) with an ideal discretization matrix,  $\mathbf{A}_{id}$ , as discussed in Section 2.2.3.
6. Determine free parameters of irregular FD stencils that use the boundary information (in step 3) by minimizing  $|\mathbf{E}|_2$  following the optimization procedure outlined in Section 2.2.3 and Appendix B.

### Appendix D. Truncation error study of pressure and temperature extrapolation operators

An important part of the immersed boundary method is the extrapolation procedure of the pressure and temperature values to the immersed boundary so that flux boundary conditions can be applied. The following study was carried out to investigate the effect of the WLSQR and the WLSQR+ extrapolation schemes for the pressure and temperature boundary conditions (see Section 2.2.4) on the accuracy of the overall immersed scheme.

Both extrapolation schemes were implemented to obtain formally arbitrary orders of accuracy. In the present study, however, only the second-order accurate (WLSQR2/WLSQR+2) and third-order accurate (WLSQR3/WLSQR+3) schemes were considered. For the WLSQR+ scheme no additional grid points ( $n_A = 0$ ) were used to calculate the extrapolation stencils (see Eq. (18)). The results of the presented truncation error study were obtained on a uniform grid. For the error convergence study of the immersed boundary method, the location of the immersed boundary is given analytically to eliminate possible inaccuracies in the boundary representation. The exact pressure values on the immersed boundary can be computed utilizing Eq. (25).

The accuracy of the different extrapolation schemes is evaluated by computing the difference of the extrapolated pressure boundary condition and the exact pressure on the boundary. In addition, the effect of the extrapolation schemes on the accuracy of the discrete convective operator is investigated by computing the truncation error of the flow field around a

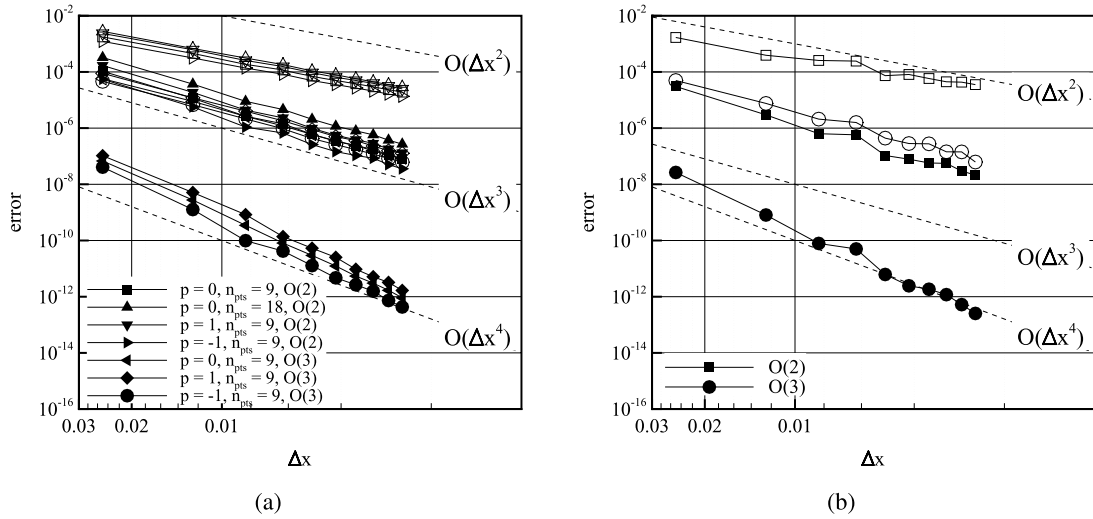


**Fig. D.24.** Pressure boundary condition extrapolation error in  $L_\infty$ -norm ( $\square, \triangle, \nabla, \triangleright, \triangleleft, \diamond, \circ$ ) and  $L_2$ -norm ( $\blacksquare, \blacktriangle, \blacktriangledown, \blacktriangleright, \blacktriangleleft, \blacklozenge, \bullet$ ): (a) WLSQR and (b) WLSQR+.

cylinder. Different exponents for the weights of the WLSQR scheme are tested. The weights,  $w_k$ , for the WLSQR schemes are controlled by defining an exponent  $p$  as introduced in Eq. (19). The error convergence of the different extrapolation schemes are shown in Figs. D.24(a) and D.24(b). The exponent  $p$  of the weights in the weighted least-squares procedure has some effect on the accuracy of the pressure boundary condition. With increasing values of  $p$ , the error becomes slightly larger. Contrary to common practice, a negative value of  $p$  was also tested. In situations where an irregular grid point is very close to the immersed boundary, negative values of  $p$  may be used to reduce the condition number of the system of equations. For the WLSQR+ scheme, the exponent  $p$  has no effect on the accuracy since in the current study the minimum number of points required to obtain the desired order of accuracy ( $n_A = 0$ ) is chosen. As one may expect, the stencil size has also an effect on the accuracy. The extrapolation error becomes larger when increasing the number of grid points in the extrapolation stencil from  $n_{pts} = 9$  to  $n_{pts} = 18$ . The formal order of accuracy of the second-order and third-order extrapolation schemes can be verified in Figs. D.24(a) and D.24(b).

## Appendix E. Stretching functions

The 3rd-order polynomial stretching is of the form

$$x_i(\xi_i) = a\xi_i^3 + b\xi_i^2 + c\xi_i + d, \quad (\text{E.1})$$

where  $x_i$  denote the physical and  $\xi_i$  the computational coordinates. The following conditions are used to determine the constants of the stretching polynomial

- $x_0 = \xi_0$ ,
- $x_1 = \xi_1$ ,
- $\Delta x(x_c) = \Delta x_{\min}$ , and
- $\Delta \xi / \Delta x_{\min} = \beta$ ,

where the index 0 indicates the beginning of the domain and index 1 denotes the domain end. The location  $x_c$  determines the location in physical space where the grid spacing has a minimum. The factor  $\beta$  determines the ratio between the spacing of the uniform computational grid to the finest grid spacing in the physical domain. Wavy grid transformation in 2D:

$$\begin{aligned} x(\xi, \eta) &= \xi + A_x \sin\left(\frac{\pi n_{xy} \eta}{L_y}\right), \text{ and} \\ y(\xi, \eta) &= \eta + A_y \sin\left(\frac{\pi n_{yx} \xi}{L_x}\right). \end{aligned} \quad (\text{E.2})$$

Wavy grid transformation in 3D:

$$\begin{aligned} x(\xi, \eta, \zeta) &= \xi + A_x \sin\left(\frac{\pi n_{xy} \eta}{L_y}\right) \sin\left(\frac{\pi n_{xz} \zeta}{L_z}\right), \\ y(\xi, \eta, \zeta) &= \eta + A_y \sin\left(\frac{\pi n_{yx} \xi}{L_x}\right) \sin\left(\frac{\pi n_{yz} \zeta}{L_z}\right), \text{ and} \end{aligned}$$

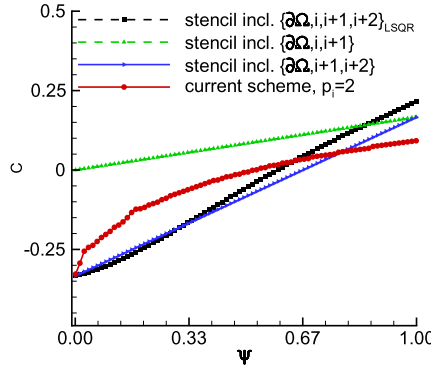


Fig. F.25. Comparison of factor,  $C$ , of leading order truncation error at  $x_i$  for different immersed schemes.

Table F.3

Factor,  $C$ , of leading order truncation error,  $\tau|_i = C \Delta x^{p_i} \frac{\partial^{p_i+1} \phi}{\partial x^{p_i+1}}|_i$ , for different immersed schemes.

Stencil incl. $\{\partial\Omega, i, i+1, i+2\}_{LSQ}$	Stencil incl. $\{\partial\Omega, i, i+1\}$	Stencil incl. $\{\partial\Omega, i+1, i+2\}$	Current scheme ( $p_i = 2, 3$ )
$\frac{-8+\psi(1+\psi)(2+\psi)(3+2\psi)(-1+3\psi)}{6(4+3\psi(1+\psi)^2(2+\psi))}$	$\frac{\psi}{6}$	$\frac{-2+3\psi}{6}$	$\frac{\psi+2c_{i+2}(2+\psi)\Delta x}{6}$ $\frac{-\psi+3c_{i+3}(3+\psi)\Delta x}{12}$

$$z(\xi, \eta, \zeta) = \eta + A_z \sin\left(\frac{\pi n_{zx}\xi}{L_x}\right) \sin\left(\frac{\pi n_{zy}\eta}{L_z}\right). \quad (\text{E.3})$$

Here, the constants are chosen as  $A_x = A_y = A_z = 0.05$  and  $n_{xy} = n_{yx} = n_{xz} = n_{zx} = n_{yz} = n_{zy} = 4$ .

#### Appendix F. Truncation error analysis of alternative immersed boundary methods

The accuracy between the current immersed boundary method and the alternative immersed schemes in Section 4.2 is compared by computing the truncation error at the irregular grid point,  $x_i$ , considering equidistant grid spacings. The truncation error,  $\tau$ , is obtained by

$$\tau|_i = \frac{\partial \phi}{\partial x}\bigg|_i - c_{\partial\Omega} \phi_{\partial\Omega} - \sum_{m=1}^{p_k+1} c_{i+m-1} \phi_{i+m-1}. \quad (\text{F.1})$$

Table F.3 lists the leading order truncation error at  $x_i$  for the current immersed boundary method, and the three alternative immersed schemes. The truncation errors depend on the boundary distance,  $\psi$ , and the free parameter,  $c_{i+p_i}$ , of the current immersed scheme. It can be noted that the truncation error of the current second-order accurate scheme contains the same factor  $C$  as the second alternative scheme plus a term containing the free parameter,  $c_{i+p_i}$ . This term (although it is multiplied by  $\Delta x$ ) is part of the leading order truncation error because for the first derivative the FD stencil coefficients,  $c_{i+m-1}$ , scale with the inverse of the grid spacing. Fig. F.25 provides a comparison of the local truncation error at irregular grid point  $x_i$  for different second-order accurate immersed schemes by plotting factor,  $C$ , and considering the optimal coefficient,  $c_{i+2}$ , for the current immersed scheme shown in Fig. B.23(b). It appears that the second alternative scheme is slightly more accurate than the current second-order accurate immersed scheme for small boundary distances. Note, that the second alternative scheme becomes singular in the limit of  $\psi$  approaching zero because the grid line intersection point and the irregular grid point  $x_i$  collapse. Moreover, as shown in Section 4.2 and Appendix G none of the three alternative schemes is stable for all  $\psi$ . Most importantly, the current immersed scheme can also be made higher-order accurate.

#### Appendix G. Two dimensional matrix stability analysis

For the 2D linear stability analysis, a circle with a diameter  $D = 0.5$  located at  $(x_0, y_0) = (0, 0)$  was immersed into a unit square computational domain. The flow field was set to the potential flow solution around a cylinder.

$$\begin{aligned} \rho(x, y) &= \rho_\infty, \\ u(x, y) &= \frac{U_\infty}{r^2} \left[ (x-x_0)^2 \left( 1 - \frac{R_0^2}{r^2} \right) + (y-y_0)^2 \left( 1 + \frac{R_0^2}{r^2} \right) \right], \\ v(x, y) &= \frac{U_\infty}{r^2} \left[ (x-x_0)(y-y_0) \left( 1 - \frac{R_0^2}{r^2} \right) - (x-x_0)(y-y_0) \left( 1 + \frac{R_0^2}{r^2} \right) \right], \end{aligned}$$



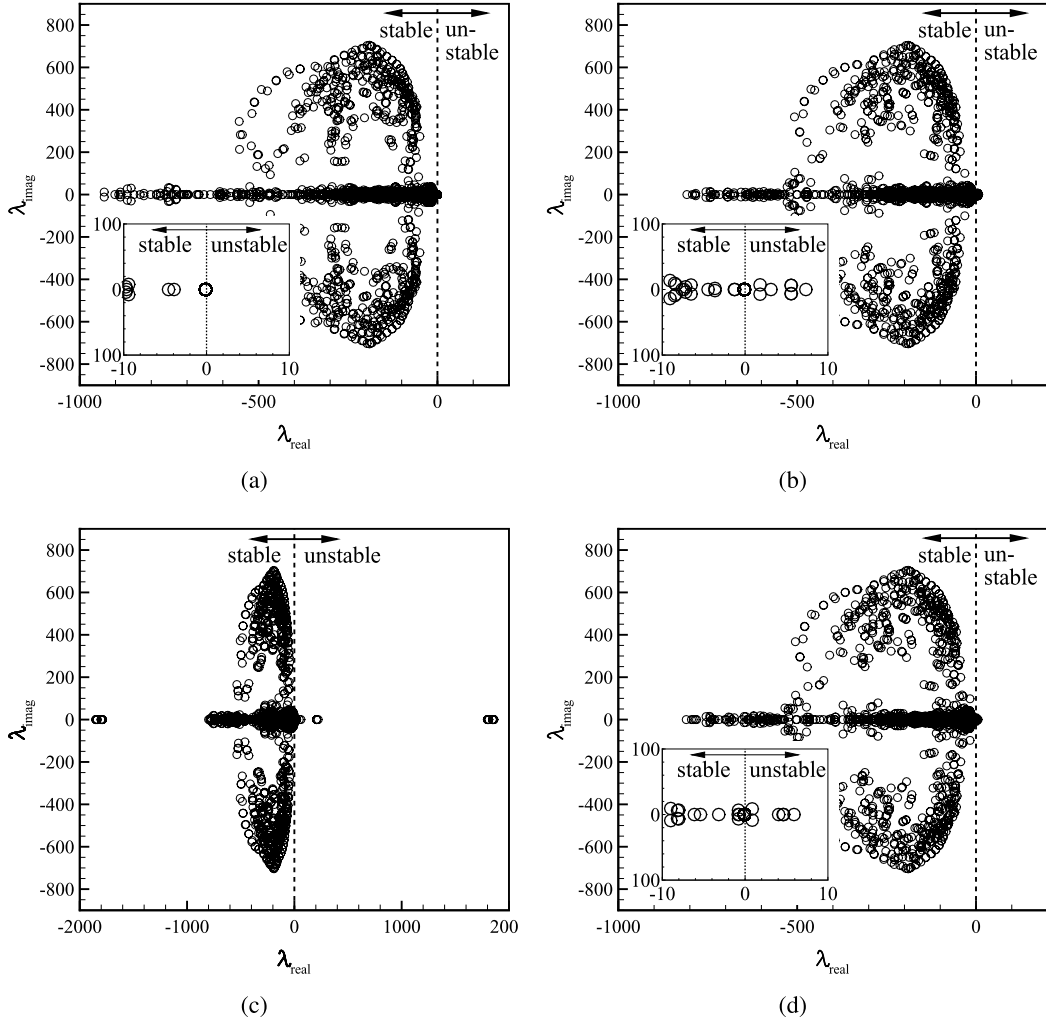


**Fig. G.26.** Stability analysis of spatial discretization matrix for (a) current immersed boundary method, (b) excluding grid point  $i$ , (c) excluding grid point  $i + 2$ , and (d) applying LSQR considering all grid points.

$$p(x, y) = \frac{1}{2} \rho_{\infty} \left( U_{\infty}^2 - \left[ u(x, y)^2 + v(x, y)^2 \right] \right), \text{ and}$$

$$T(x, y) = \frac{p(x, y)}{R \rho(x, y)}, \quad (\text{G.1})$$

where  $r = \sqrt{(x - x_0)^2 + (y - y_0)^2}$  is the local radius in the Cartesian coordinate system,  $R_0 = D/2$  is the cylinder radius, and  $(x_0, y_0)$  denote the center of the cylinder. The free-stream flow conditions are  $U_{\infty} = 34.72$ ,  $V_{\infty} = 0$ ,  $p_{\infty} = 101327$ ,  $T_{\infty} = 300$  and the ideal gas properties are  $\gamma = 1.4$ ,  $c_p = 1005$  and  $R = 287$ .

The same immersed boundary methods as in Section 4.2 for 1D stability analysis were compared to each other. Three different mesh sizes with  $N = 20, 40$ , and  $80$  were considered in this investigation. Only the results for  $N = 20$  are shown here since the same conclusions can be drawn for all three grid resolutions. The stability analysis results of the spatial discretization matrix for the four methods are shown in Fig. G.26(a)–(d). For all three alternative immersed boundary schemes in Fig. G.26(b)–(d), some eigenvalues appear in the right half plane of the complex plane indicating that all other immersed boundary methods are linearly unstable for this setup. When visualizing the eigenfunctions associated with the least stable eigenvalue for the different schemes it was noted that the maxima in the eigenfunction occurs at different irregular grid points. The stability analysis results for the update matrix are displayed in Fig. G.27(a)–(d). As for the stability analysis of the spatial operator, all other immersed boundary methods are unstable since some of the eigenvalues are located outside the unit circle.

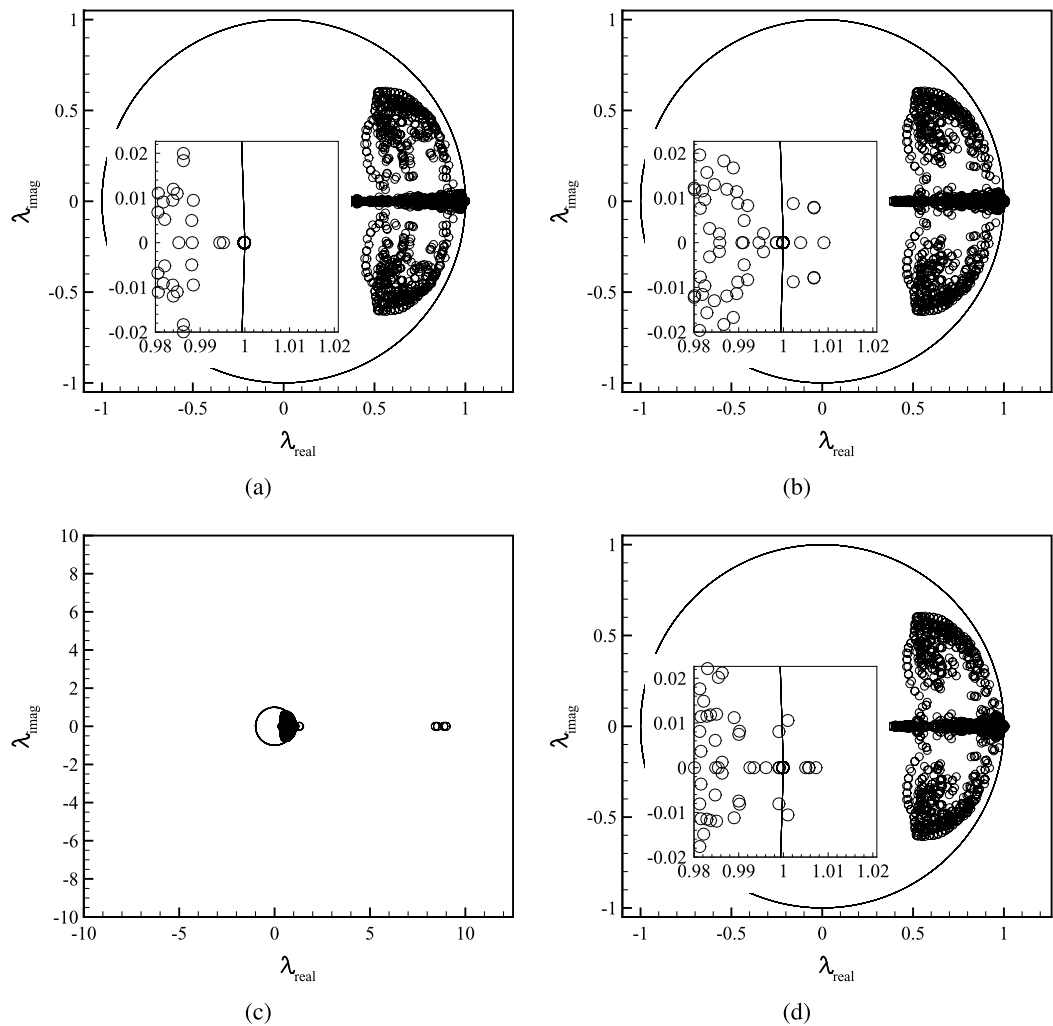


**Fig. G.27.** Stability analysis of the update matrix for (a) current immersed boundary method, (b) excluding grid point  $i$ , (c) excluding grid point  $i + 2$ , and (d) applying LSQR considering all grid points.

**Appendix H. Flow conditions and simulation setups**

**Table H.4**  
Computational setup and flow conditions for cylinder/sphere simulations.

Parameter	Value (cylinder)	Value (sphere)
domain size	$(L = 80D, H = 80D)$	$(L = 16D, H = 16D, W = 16D)$
center of cylinder/sphere $x_0, y_0, z_0$	$25D, 40D$	$4D, 8D, 8D$
domain length	$L = 80D$	$L = 16D$
domain height	$H = 80D$	$H = 16D$
domain width	—	$W = 16D$
CFL-number	$\approx 1$	$\approx 1$
time integration	RK $\mathcal{O}(\Delta t^4)$	RK $\mathcal{O}(\Delta t^4)$
Inflow BC	Velocity Inlet	Velocity Inlet
Outflow BC	Outlet	Outlet
Top/bottom BC	Extrapolation	Extrapolation
Front/back BC	—	Extrapolation
$U_\infty$	34.7 m/s	34.7 m/s
$V_\infty$	0 m/s	0 m/s
$\rho_\infty$	1.1762 kg/m <sup>3</sup>	1.1762 kg/m <sup>3</sup>
$T_\infty$	300 K	300 K
$p_\infty$	101 327 Pa	101 327 Pa

**Table H.4** (Continued)

Parameter	Value (cylinder)	Value (sphere)
$\gamma$	1.4	1.4
$c_p$	1005 J/(kg K)	1005 J/(kg K)
$D$	1 m	1 m
$\mu$	$\rho_\infty U_\infty D / Re_D$	$\rho_\infty U_\infty D / Re_D$

**Table H.5**

Flow conditions for the porous wall simulations.

Parameter	Value
$M$	6.0
$T_\infty$	216.65 K
$L_{ref}$	$\delta^*$
$\gamma$	1.4
$Pr$	0.72
$T_w / T_\infty$	7.027
$Re_{\delta^*}$	20 000
$x_{inflow}$	114.92 $\delta^*$
$\alpha_r$	3.0 $\delta^*$
$\omega_r$	1.195

**Table H.6**

Flow conditions for discrete roughness simulations.

Parameter	Value
domain size	$L = 180\delta^*, H = 180\delta^*$
$\rho_\infty$	1.1762 kg/m <sup>3</sup>
$p_\infty$	101 327 Pa
$T_\infty$	300 K
$L_{ref}$	$\delta^*$
$M$	0.1
$Re_{\delta^*}$	164.57
$x_{inflow}$	15 $\delta^*$
$\gamma$	1.4
$Pr$	0.72
$CFL$	$\approx 0.5$

## References

- [1] C. Peskin, Numerical analysis of blood flow in the heart, *J. Comput. Phys.* 25 (1977) 220–252.
- [2] C.S. Peskin, The immersed boundary method, in: *Acta Numerica*, Cambridge University Press, 2002, pp. 1–39.
- [3] D. Goldstein, R. Handler, L. Sirovich, Modeling a non-slip flow boundary with an external force field, *J. Comput. Phys.* 105 (1993) 354–366.
- [4] R.J. LeVeque, Z. Li, The immersed interface method for elliptic equations with discontinuous coefficients and singular sources, *SIAM J. Numer. Anal.* 31 (4) (1994) 1019–1044.
- [5] A. Wiegmann, K. Bube, The explicit-jump immersed interface method: finite difference methods for PDEs with piecewise smooth solutions, *SIAM J. Numer. Anal.* 31 (4) (1992) 1019–1044.
- [6] M. Linnick, H. Fasel, A high-order immersed interface method for simulating unsteady incompressible flows on irregular domains, *J. Comput. Phys.* 204 (2004) 157–192.
- [7] H. Johansen, P. Collela, A Cartesian grid embedded boundary method for Poisson's equation on irregular domains, *J. Comput. Phys.* 147 (1998) 60–85.
- [8] R. Mittal, G. Iaccarino, Immersed boundary methods, *Annu. Rev. Fluid Mech.* 37 (2005) 239–261.
- [9] X. Zhong, A new high-order immersed interface method for solving elliptic equations with embedded interface of discontinuity, *J. Comput. Phys.* 225 (2007) 1066–1099.
- [10] L. Duan, X. Wang, X. Zhong, A high-order cut-cell method for numerical simulation of hypersonic boundary-layer instability with surface roughness, *J. Comput. Phys.* 229 (2010) 7207–7237.
- [11] C. Kiris, M. Barad, J. Housman, H. Sozer, C. Brehm, S. Moni-Yekta, The LAVA Computational Fluid Dynamics Solver, AIAA Science and Technology Forum and Exposition, 2014.
- [12] M. Nemec, M. Aftosmis, Aerodynamic shape optimization using a Cartesian adjoint method and CAD geometry, in: 24th AIAA Applied Aerodynamics Conference, 2006, AIAA 2006-3456.
- [13] R. Mittal, H. Dong, M. Bozkurtas, F. Najjar, A. Vargas, A. von Loebbecke, A versatile sharp interface immersed boundary method for incompressible flows with complex boundaries, *J. Comput. Phys.* 227 (2008) 4825–4852.
- [14] J. Ferziger, M. Peric, *Computational Methods in Fluid Dynamics*, Springer-Verlag, New York, 1996.
- [15] T. Tezduyar, Finite element methods for flow problems with moving boundaries and interfaces, *Arch. Comput. Methods Eng.* 8 (2001) 83–130.
- [16] C. Brehm, H.F. Fasel, Novel immersed interface method based on local stability condition, in: 40th Fluid Dynamics Conference and Exhibit, 2010, AIAA-2010-4432.
- [17] C. Brehm, H.F. Fasel, A non-staggered immersed interface method for solving the incompressible Navier–Stokes equations, in: 40th Fluid Dynamics Conference and Exhibit, 2010, AIAA-2010-4433.
- [18] Z. Li, K. Ito, *The Immersed Interface Method: Numerical Solutions of PDEs Involving Interfaces and Irregular Domains*, SIAM Book, 2006.
- [19] J.H. Seo, R. Mittal, A high-order immersed boundary method for acoustic wave scattering and low-Mach number flow-induced sound in complex geometries, *J. Comput. Phys.* 230 (4) (2011) 1000–1019.
- [20] C. Brehm, H. Fasel, A novel concept for the design of immersed interface methods, *J. Comput. Phys.* 242 (2013) 234–267, <http://dx.doi.org/10.1016/j.jcp.2013.01.027>, <http://www.sciencedirect.com/science/article/pii/S0021999113000715>.
- [21] C. Brehm, H.F. Fasel, Immersed interface method for solving the incompressible Navier–Stokes equations with moving boundaries, in: 49th AIAA Aerospace Sciences Meeting, 2011, AIAA-2011-0758.
- [22] A.C. Laible, H.F. Fasel, Temporal direct numerical simulations of oblique breakdown for a cone at Mach 3.5, in: 49th AIAA Aerospace Sciences Meeting, 2011, 2011-0209.
- [23] X. Zhong, High-order finite-difference schemes for numerical simulation of hypersonic boundary-layer transition, *J. Comput. Phys.* 144 (1998) 662–709.
- [24] M. Visbal, D. Gaitonde, High-order accurate methods for unsteady vortical flows on curvilinear meshes, in: 36th AIAA Aerospace Sciences Meeting and Exhibit, 1998, AIAA 1998-0131.
- [25] C. Shu, S. Osher, Efficient implementation of essentially non-oscillatory shock-capturing schemes, *J. Comput. Phys.* 77 (2) (1988) 439–471.
- [26] C. Brehm, M. Barad, J. Housman, C. Kiris, A comparison of higher-order shock capturing schemes, *Comput. Fluids* (2015), submitted for publication.
- [27] T. Nonomura, N. Iizuka, K. Fujii, Freestream and vortex preservation properties of high-order WENO and WCNS on curvilinear grids, *Comput. Fluids* 39 (2010) 197–214.
- [28] B. van Leer, Flux-vector splitting for the Euler equations, in: *International Conference on Numerical Methods in Fluid Dynamics*, vol. 170, 1982, pp. 507–512.

- [29] H. Luo, R. Mittal, X. Zheng, S.A. Bielałowicz, R.J. Walsh, J.K. Hahn, An immersed-boundary method for flow-structure interaction in biological systems with application to phonation, *J. Comput. Phys.* 227 (22) (2008) 9303–9332.
- [30] N. Adams, K. Shariff, A high-resolution hybrid compact-eno scheme for shock-turbulence interaction problems, *J. Comput. Phys.* 127 (1) (1996) 27–51.
- [31] I. Gelfand, Normierte ringe, *Rec. Math. [Mat. Sbornik] N.S.* 9 (51) (1941) 3–24.
- [32] E.M. Saiki, S. Biringen, Numerical simulation of a cylinder in uniform flow: application of virtual boundary method, *J. Comput. Phys.* 123 (1996) 450–465.
- [33] D. Calhoun, A Cartesian grid method for solving the two-dimensional streamfunction-vorticity equations in irregular regions, *J. Comput. Phys.* 176 (2) (2002) 231–275.
- [34] D.J. Tritton, Experiments on the flow past a circular cylinder at low Reynolds numbers, *J. Fluid Mech.* 6 (1959) 547–567.
- [35] M. Behr, D. Hastreiter, S. Mittal, T.E. Tezduyar, Incompressible flow past a circular cylinder: dependence of the computed flow field on the location of the lateral boundaries, *Comput. Methods Appl. Mech. Eng.* 135 (1995) 309–316.
- [36] B. Fornberg, A numerical study of steady viscous flow past a circular cylinder, *J. Fluid Mech.* 98 (1980) 819–855.
- [37] S.C.R. Dennis, G.Z. Chang, Numerical solutions for steady flow past a circular cylinder at Reynolds numbers up to 100, *J. Fluid Mech.* 42 (1970) 471–489.
- [38] M. Coutanceau, R. Bouard, Experimental determination of the main features of the viscous flow in the wake of a circular cylinder in uniform translation. Part 1, Steady flow, *J. Fluid Mech.* 79 (1977) 231–256.
- [39] R.D. Henderson, Details of the drag curve near the onset of vortex shedding, *Phys. Fluids* 7 (9) (1995) 2102–2104.
- [40] S. Marella, S. Krishnan, H. Liu, H. Udaykumar, Sharp interface Cartesian grid method I: an easily implemented technique for 3D moving boundary computations, *J. Comput. Phys.* 210 (2005) 1–31.
- [41] E. Berger, R. Wille, Periodic flow phenomena, *Annu. Rev. Fluid Mech.* 79 (1972) 313–340.
- [42] C. Liu, X. Zheng, C.H. Sung, Preconditioned multigrid methods for unsteady incompressible flows, *J. Comput. Phys.* 139 (1998) 35–57.
- [43] A. Belov, L. Martinelli, A. Jameson, A new implicit algorithm with multigrid for unsteady incompressible flow calculations, in: *AIAA 33rd Aerospace Sciences Meeting*, Reno, NV, 1995, AIAA paper 95-0049.
- [44] T.A. Johnson, V.C. Patel, Flow past a sphere up to a Reynolds number of 300, *J. Fluid Mech.* 378 (1999) 19–70.
- [45] S. Taneda, Experimental investigation of the wake behind a sphere at low Reynolds numbers, *J. Phys. Soc. Jpn.* 30 (1) (1956) 1104–1108.
- [46] N.D. Sandham, H. Lüdeke, A numerical study of Mach 6 boundary layer stabilization by means of a porous surface, 2009, *AIAA 2009-1288*.
- [47] C. Hader, H.F. Fasel, Numerical investigation of porous walls for a Mach 6.0 boundary layer using an immersed boundary method, in: *41st AIAA Fluid Dynamics Conference and Exhibit*, 2011, AIAA-2011-3081.
- [48] N.D. Malmuth, A.V. Fedorov, D. Marshall, Ultrasonically Absorptive Coatings for Hypersonic Laminar Flow Control, 2008.
- [49] A.V. Fedorov, N.D. Malmuth, A. Rasheed, H.G. Hornung, Stabilization of hypersonic boundary layers by porous coatings, *AIAA J.* 39 (4) (2001).
- [50] A.V. Fedorov, V. Kozlov, A. Shiplyuk, A. Maslov, N.D. Malmuth, Stability of hypersonic boundary layer on porous wall with regular microstructure, *AIAA J.* 44 (8) (2006) 1866–1871.
- [51] G. Brès, T. Colonius, A.V. Fedorov, Stability of temporally evolving supersonic boundary layers over micro-cavities for ultrasonic absorptive coatings, 2008, *AIAA 2008-4337*.
- [52] A.V. Fedorov, Temporal stability of hypersonic boundary layer on porous wall: comparison of theory with DNS, 2010, *AIAA 2010-1242*.
- [53] V. Wartemann, H. Lüdeke, N.D. Sandham, Stability analysis of hypersonic boundary layer flow over microporous surfaces, in: *16th AIAA/DLR/DGLR International Space Planes and Hypersonic Systems and Technologies Conference*, 2009.
- [54] C. Hader, C. Brehm, H.F. Fasel, Numerical investigation of porous walls for a Mach 6.0 boundary layer using an immersed interface method, 2013, *AIAA 2013-0829*.
- [55] C. Hader, C. Brehm, H.F. Fasel, Numerical investigation of transition delay in a Mach 6 boundary layer using porous walls, 2013, *AIAA 2013-2740*.